STUDIES OF A POLOIDAL DIVERTOR REVERSED FIELD PINCH

by

JOHN STEPHEN SARFF

A thesis submitted in partial fulfillment of the
requirements for the degree of

Doctor of Philosophy
(Physics)

at the
UNIVERSITY OF WISCONSIN–MADISON
1988

STUDIES OF A POLOIDAL DIVERTOR REVERSED FIELD PINCH

John Stephen Sarff

Under the supervision of Professor Julien Clinton Sprott

Several attempts have been made to form a reversed field pinch (RFP) in a four-node, poloidal divertor configuration which positions the plasma far from a conducting wall. In this configuration, the plasma is localized within a magnetic separatrix formed by the combination of toroidal currents in the plasma and four, internal, conducting rings.

These experiments were conducted on three devices: Tokapole II, the Wisconsin Levitated Octupole, and the modified Octupole with smaller conducting rings. Transient, RFP-like equilibria were obtained on Tokapole II and the Wisconsin Levitated Octupole. RFP-like equilibria with field reversal duration ~1 msec were obtained on the small ring Octupole. None of these plasmas was sustained against resistive magnetic diffusion.

Local, internal measurements of the magnetic field in Tokapole II plasmas indicated the plasma current and density were mostly confined to the region inside the magnetic separatrix. The sharp drop in plasma pressure near the separatrix generated a large diamagnetic current in that region.

Large magnetic perturbations were observed in the startup phase of these plasmas. On the small ring Octupole, the perturbation ($\delta B/B$~40%) was measured to have a dominant poloidal mode number of m=1 and toroidal mode numbers n~−5, *i.e.*, internally resonant or nonresonant modes. This perturbation was stationary and was phase-locked to a magnetic field error.

If the tenuous plasma region outside the separatrix is "vacuum-like," then this behavior might represent current-driven instability owing to the lack of a nearby, stabilizing boundary. Such instability is consistent with linear magnetohydrodynamic stability calculations and nonlinear simulations of a cylindrical RFP plasma bounded by a large vacuum region and a distant conducting wall.

ACKNOWLEDGMENTS

I would like to thank my advisor, Professor Sprott, for his enthusiastic support and guidance during the course of this research and throughout my graduate career. I would also like to thank Professor Prager and Professor Dexter for their suggestions, insight, and continued interest in this work. I would like to give special thanks to Dr. Leaf Turner for his help obtaining the force-free equilibrium solutions in the four-node poloidal divertor geometry while on leave at Wisconsin.

Without the efforts of John Laufenberg, Tom Lovell, Jim Morin and a host of hourly workers, who provided vital technical support and expertise in the development of diagnostics and in the general maintenance of Tokapole II and the Octupole, this work would not have been possible.

I am greatly indebted to my fellow graduate students who often provided their labor for my benefit and who made graduate student life a pleasurable experience. I am especially grateful to Saeed Assadi and Abdulgader Almagri for their assistance in the final days of the Octupole when time and energy ran short, and to Bill Ho for many elucidative discussions on the nature of the nonideal RFP boundary.

Finally, I express my greatest appreciation for my parents, Don and Marilyn, whose love, support, and encouragement have helped make this success.

This work was financially supported by the U.S. Department of Energy, and was performed, in part, under appointment to the U.S. Department of Energy Magnetic Fusion Energy Technology Fellowship program which is administered for DOE by Oak Ridge Associated Universities.

CONTENTS

CHAPTER 1

INTRODUCTION

The reversed field pinch[1,2,3] has great potential as a viable magnetic fusion plasma confinement system with many advantageous characteristics. For example, a reversed field pinch (RFP) fusion plasma can be purely ohmically heated since the plasma current is not constrained below the Kruskal-Shafranov limit. Also, the large magnetic shear inherent in the RFP allows operation with large β, *i.e.*, the ratio of plasma thermal pressure to magnetic pressure, so an RFP fusion reactor would operate economically with high power density. But some components in every fusion plasma confinement systems challenge fusion engineering. In the RFP, the predicted requirement of a close-fitting, highly conductive wall—fundamental to both magnetohydrodynamic (MHD) stability[4,5] and RFP relaxation theory[6]—imposes severe constraints on RFP reactor design.[7] To understand this important issue, a surge of theoretical and experimental research on the physics of the RFP electrical boundary condition has recently begun.

The RFP electrical boundary consists primarily of two parameters: the shell resistive time constant, $\tau_s = \mu_0 a \Delta / \eta_s$, and the extent of the vacuum layer between the plasma and the shell. The resistive time constant depends on the shell material resistivity, η_s, the shell thickness, Δ, and the plasma radius, a. Most RFP devices have been constructed with highly conductive shells, *e.g.*, aluminum or copper, and minimal vacuum layers.

Recent experiments,[8,9,10] though, are investigating the effect of a small resistive shell time compared with the plasma duration. The push for thin shell design was spurred on by optimistic results from the OHTE device at General Atomics which achieved 15 msec pulse-lengths using a brass shell with a resistive time constant of 1.5 msec.[11] To investigate the dependence on the vacuum layer thickness, experiments are proposed for MST, the new device at the University of Wisconsin-Madison, in which movable limiters will vary the vacuum layer thickness.[12]

This thesis describes three attempts to form an RFP plasma in a four-node, poloidal divertor configuration. In this configuration, a magnetic separatrix limits the plasma current and density far from a conducting wall. If the tenuous plasma region outside the separatrix is "vacuum-like," then a large "vacuum" layer bounds the RFP formed within the separatrix. The "vacuum" layer thickness is not adjustable, as proposed in the MST experiments, but for the cases examined in this thesis, it is larger than in any past or present RFP experiment (except, perhaps, Multipinch[13] at General Atomics).

The usual interest in magnetic divertors relates to particle and impurity control at the plasma boundary as envisioned in a fusion reactor. This thesis, however, focuses on the behavior of an RFP located far from a stabilizing wall. Since such equilibria might be unstable, measurements of the equilibrium and stability properties of the poloidal divertor configuration are emphasized.

The three, four-node poloidal divertor configurations examined in this work are shown schematically in Fig. 1-1. The first experiments were

performed on the Tokapole II device (Fig. 1-1a), normally operated as a poloidal divertor tokamak. Transient, RFP-like equilibria were obtained, and the equilibrium magnetic field profiles were measured. The plasma current density profiles inferred from the magnetic field measurements indicated that, indeed, the magnetic separatrix acted to limit the plasma current and pressure.

To overcome the small-size limitations of Tokapole II, most notably the large required toroidal loop voltage, the poloidal divertor RFP experiment was attempted in the the large Wisconsin Levitated Octupole (Fig. 1-1b); the results resembled those obtained in Tokapole II. Arcing of the high voltage poloidal gap, which was exposed to the plasma, prompted the removal of the divertor rings to facilitate the development of a suitable protection scheme. For about one year thereafter, large noncircular RFP plasmas were studied in the divertorless Levitated Octupole vacuum vessel (Fig. 1-1c), and the results are reported elsewhere.[14]

A return to the poloidal divertor RFP experiment began with the installation of new divertor rings in the old Octupole vacuum vessel (Fig. 1-1d). The new rings, which were smaller than the originals, allowed a larger ratio of plasma current to ring current. The plasmas obtained in this device were most interesting. The duration of reversal exceeded those previously obtained, although sustainment was not observed. Also, a large, stationary, global asymmetry in the magnetic field set in about the time when the spatially averaged toroidal field reversed at the wall.

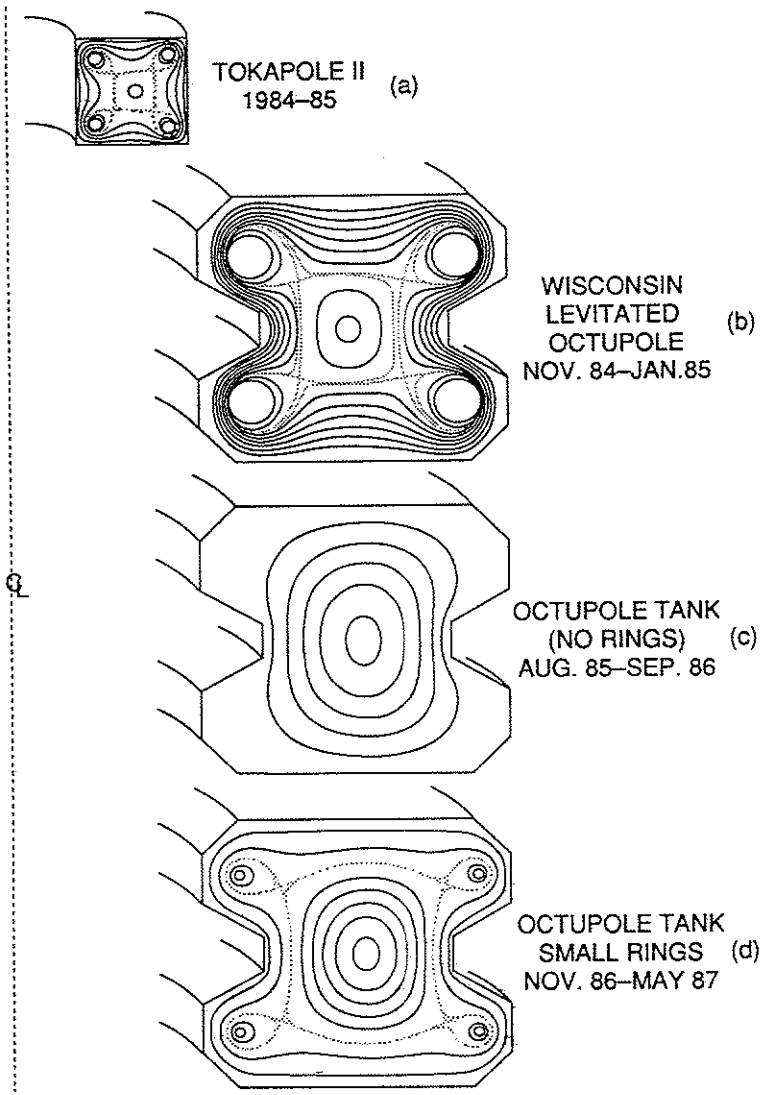

Fig. 1-1. Four-node poloidal divertor configurations.

This thesis is organized in five chapters. Chapter 2 briefly reviews the MHD equilibrium and stability properties of the RFP, particularly the standard circular RFP. Chapter 3 includes device descriptions and information about the primary diagnostics used in this research. Chapter 4 presents the experimental results, and Chapter 5 summarizes the results and conclusions.

Since toroidal effects are small in the RFP, many theorists use straight cylindrical geometry with coordinates r,θ, and z. Often the toroidal angular coordinate "ϕ" is substituted for "z," particularly in subscripting variables, without the inclusion of toroidal effects. In this thesis, "ϕ" indicates both "toroidal" and "axial"; a comment will be made when toroidal effects are included.

Occasional references are made to PLP reports. These informal reports are circulated internally within the University of Wisconsin-Madison Plasma Physics Group and are available upon request from:

Plasma Physics Department

University of Wisconsin-Madison

1150 University Ave.

Madison, WI 53706

REFERENCES

1 H.A.B. Bodin and A.A. Newton, Nucl. Fusion **20**, 1255 (1980).

2 H.A.B. Bodin, Nucl. Instrum. and Methods **207**, 1 (1983).

3 D.A. Baker and W.E. Quinn, in *Fusion*, edited by E. Teller (Academic, New York, 1981), Vol. 1, Part A, Chap. 7.

4 D.C. Robinson, Plasma Physics **13**, 439 (1971).

5 D.C. Robinson, Nucl. Fusion **18**, 939 (1978).

6 J.B. Taylor, Rev. Mod. Physics **58**, 741 (1986).

7 *The Titan Reversed-Field Pinch Fusion Reactor Study*, papers presented at IEEE 12th Symposium on Fusion Engineering, Monterey, California, October 12–16, 1987, UCLA report UCLA-PPG-1110.

8 N. Asakura, A. Fujisawa, T. Fujita, Y. Fukada, H. Hattori, N. Inoue, S. Ishida, K. Itami, Y. Iwata, H. Ji, Y. Kamada, K. Kusano, S. Matsuzuka, K. Miyamoto, J. Morikawa, C. P. Munson, Y. Murakami, Y. Nagayama, H. Nihei, S. Onodera, M. T. Saito, T. Sato, S. Shinohara, H. Toyama, Y. Ueda, M. Utumi, and H. Yamada, in *Plasma Physics and Controlled Nuclear Fusion Research*, 1986 , Proceedings of the 11th International Conference, Kyoto (IAEA, Vienna, 1987), Vol. 2, p. 433.

9 S. Robertson and P. Schmid, Phys. Fluids **30**, 884 (1987).

10 B. Alper, in *Proceedings of the IEEE International Conference on Plasma Science*, Seattle, 1988 (IEEE, New York, 1988), paper 5P17.

11 R. R. Goforth, T. N. Carlstrom, C. Chu, B. Curwen, D. Graumann, P. S. C. Lee, E. J. Nilles, T. Ohkawa, M. J. Schaffer, T. Tamano, P. L. Taylor, and T. S. Taylor, Nucl. Fusion **26**, 515 (1986).

12 R. N. Dexter, D. W. Kerst, T. W. Lovell, S. C. Prager, and J. C. Sprott, Bull. Am. Phys. Soc. **29**, 1332 (1984).

13 R.J. La Haye, T.H. Jensen, P.S.C. Lee, R.W. Moore, and T. Ohkawa, Nucl. Fusion **26**, 255 (1986).

14 A. Almagri, S. Assadi, R. N. Dexter, S. C. Prager, J. S. Sarff, and J. C. Sprott, Nucl. Fusion **27**, 1795 (1987).

CHAPTER 2

A BRIEF REVIEW OF RFP EQUILIBRIUM AND STABILITY

Most RFP experiments are performed in circular cross-sectional toroidal devices. The distinctive features of RFP equilibria are that the poloidal (B_θ) and toroidal (B_ϕ) components of the magnetic field are comparable, and the toroidal component is reversed at the plasma edge with respect to its sense on-axis. Consequently, the safety factor, $q=rB_\phi/RB_\theta$, is less than one at all radii and is negative at the edge of the plasma. The strong magnetic shear produced by the radial variation of the field stabilizes the RFP plasma. One of the important properties of the RFP is the self-generation of this reversed field equilbrium, which is thought to result from a relaxation process toward a minimum energy state independent of the initial conditions and universal for all similar geometries. Also, the reversed field equilibria may be sustained against classical resistive diffusion by a "dynamo" mechanism operating in "quasi-steady-state."

To provide the context in which the poloidal divertor RFP configuration may be discussed, some basic principles of RFP equilibrium and stability are reviewed in this chapter. Complete reviews of these subjects can be found in references 1–4.

2.1 CIRCULAR RFP EQUILIBRIA

Considering a pressureless plasma with small but nonzero resistivity and bounded by a perfectly conducting wall, Taylor[3] identified a set of minimum energy equilibrium states described by

$$\nabla\times\mathbf{B}=\lambda\mathbf{B} \qquad 2\text{-}1$$

where λ is constant. The minimization was performed assuming the total magnetic helicity, defined as

$$K=\int \mathbf{A}\cdot\mathbf{B}d\tau, \qquad 2\text{-}2$$

should be invariant on the relaxation time scale. $\mathbf{A}$ is the magnetic vector potential which satisfies $\nabla\times\mathbf{A}=\mathbf{B}$. This particular constraint was conjectured by realizing that in a perfectly conducting plasma, K is invariant for any flux tube. In a slightly turbulent plasma with finite resistivity, field line reconnection is allowed, and the infinity of flux tube invariants reduces to the single constraint that the total magnetic helicity be invariant.

The solutions of Eq. 2-1 in a cylinder are well-known to be the Bessel Function Model (BFM)

$$B_\phi=B_o J_o(\lambda r),\ B_\theta=B_o J_1(\lambda r),\ B_r=0. \qquad 2\text{-}3$$

These equilibria are specified by the two parameters λ and B_o, the magnetic field strength on-axis; for $a\lambda > 2.4$ (a is the plasma radius), the toroidal magnetic field reverses direction at the edge. Examples of BFM equilibrium magnetic field profiles and experimentally measured profiles on the HBTX-1A device are plotted in Fig. 2-1. For $a\lambda > 3.2$, the lowest energy solution of Eq. 2-1 is helically symmetric.

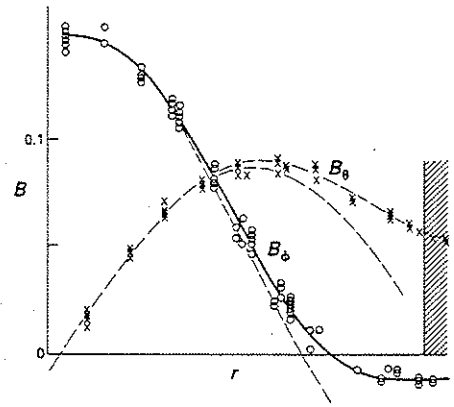

Fig. 2-1. Experimental and theoretical magnetic field profiles, HBTX-1A. (Reprinted by permission from Bodin and Taylor[3]).

Remarkably, the equilibria given by Eq. 2-1 agree well with experiment, especially by predicting reversal of the toroidal field. The model is not exact, however, and constant-λ equilibria are not fully achieved in the experiments. The deviation occurs mostly near the plasma edge where, perhaps, the large plasma resistivity hinders the relaxation process. Measured λ profiles are nearly constant in the central region of the

plasma and fall smoothly at the edge.[5,6,7] An Ohmic, force-free, paramagnetic plasma naturally exhibits non-constant-λ for realistic resistivity profiles owing to the decreasing parallel applied electric field ($\mathbf{E}\cdot\mathbf{B}/B$) in the outer region of the plasma.[8] An often-used heuristic modification of the constant-λ model which accounts for realistic profiles is the Modified Bessel Function Model (MBFM) where λ is a function of radius—constant in the central region and linearly decreasing to zero in the outer region of the plasma. This model works well in "0-D" simulations of RFP plasmas,[9] and is sometimes used to describe the equilibrium in RFP stability analysis.

Toroidal equilibrium is achieved in the RFP using a conducting wall, vertical field coils, or a combination of the two. As with the tokamak, the small horizontal displacement is given approximately by Shafranov's formula.[10] In many instances, well-centered plasmas produce optimum performance, and vertical field coils are common on present-day devices.

A steady-state, resistive, cylindrically symmetric plasma cannot exhibit field reversal by Cowling's theorem,[11] but RFP plasmas routinely endure for several resistive magnetic diffusion times in most devices. This sustainment of the reversed field equilibria by a "dynamo" mechanism is not fully understood. Models capable of predicting such behavior are based on nonlinear, resistive MHD[12] or kinetic turbulence.[13] From the viewpoint of RFP reactor development, sustainment is attractive because it allows the possibility of steady-state operation, but the "dynamo" mechanism dissipates energy and requires fluctuations which probably deleteriously affect confinement.

2.2 CONSTANT-λ EQUILIBRIA IN THE FOUR-NODE POLOIDAL DIVERTOR

The equilibria of Eq. 2-1 describe the salient features of a number of configurations, including the RFP, spheromak,[14,15] and Multipinch.[16] It is natural to ask what is the nature of the constant-λ equilibria in the four-node poloidal divertor configuration. Using analytic techniques developed by Turner,[15] the solutions of Eq. 2-1 in a straight, rectangular cross-sectional geometry allowing for the inclusion of filamentary current sources were obtained.[17] This geometry, specialized to the case of a square cross section, represents an idealization of the toroidal Tokapole II device (Fig. 3-1, pg. 25). Fig. 2-2 shows several contour plots of the axial magnetic field component, B_ϕ, obtained from the solution described in reference 17. These contours are poloidal flux surfaces, although the poloidal flux increment between surfaces is not constant. In this sequence of figures, a magnetic separatrix forms which moves closer to the filaments with the increase of λ. Profiles of B_ϕ along three chords for the case $a\lambda$=3.0 are shown in Fig. 2-3.

Because the current density is directly proportional to the field in a force-free equilibrium ($\mu_0 J=\lambda B$), the peaking of B near the current filaments implies large plasma currents flow in that region. The applied electric field in the experiment, however, is dominantly toroidal, and little ohmic power is dissipated in the "private" flux regions near the divertor rings or in the "common" flux region (composed of the field lines which link all the currents) where the magnetic field is mostly poloidal. The plasma in these regions is colder and more resistive than the plasma

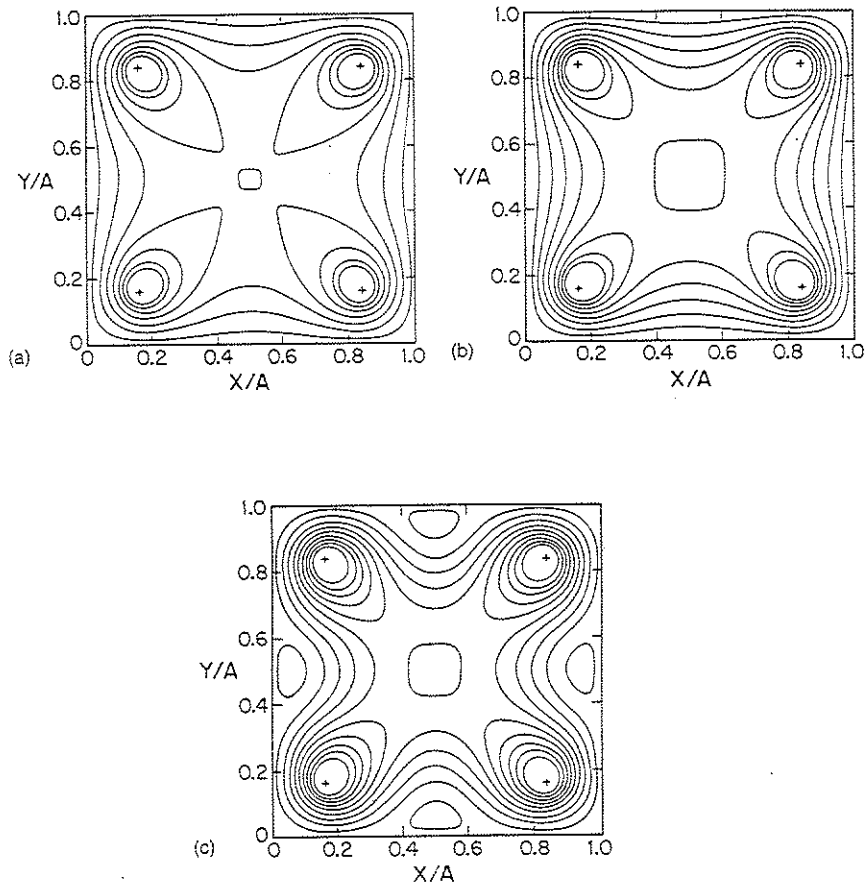

Fig. 2-2. Contours of B_ϕ in a square (a=44 cm) with four filaments, each carrying 75 kA positioned at (0.17a,0.17a), (0.17a,0.83a), (0.83a,0.17a), and (0.83a,0.83a): (a) $a\lambda$=0.5, $B_{\phi wall}$=845 G, I_p=17 kA; (b) $a\lambda$=3.0, $B_{\phi wall}$= −385 G, I_p=62 kA; (c) $a\lambda$=10.0, $B_{\phi wall}$= −3272 G, I_p= −166 kA.

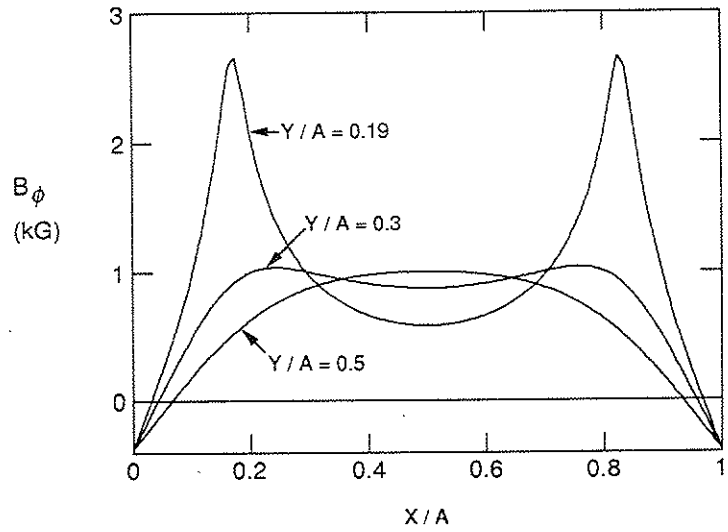

Fig. 2-3. Profiles of B_ϕ along three chords of constant y/a for $a\lambda$=3.0.

within the separatrix. Like the region near the wall in circular RFP plasmas, the "private" and "common" flux regions in the four-node poloidal divertor should be relatively current-free, and constant-λ solutions are experimentally unlikely. Indeed, measurements of the equilibrium magnetic field profiles in Tokapole II (presented in Chapter 4) imply the current density decreases sharply at the separatrix. In this sense, the separatrix magnetically limits the plasma far from the conducting wall, and the stability of the pinch discharge bounded by a large "vacuum" region is a major concern.

2.3 MHD STABILITY OF AN RFP BOUNDED BY A DISTANT CONDUCTING WALL

The linear magnetohydrodynamic stability properties of RFP equilibria are well-known.[18,19] Utilizing the energy principle and ideal MHD, possible displacements of the plasma are considered, and those which lead to a reduction in energy are unstable. Since $q<1$, stability in the RFP is achieved with a conducting wall and large magnetic shear. In general, the analysis of the equilibrium pitch, $P=rB_\phi/B_\theta=Rq$, profile indicates the type of instabilities which might be present for a given configuration. Weak shear (*e.g.*, near pitch minima) leads to instability of both pressure- and current-driven instabilities. For example, an RFP with a small vacuum region between the plasma and the conducting wall is allowed because no pitch minimum near the plasma surface is created. In contrast, a stabilized pinch configuration—similar to the RFP except the toroidal field is not quite reversed at the edge—cannot be stable with any vacuum region thickness as a result of the pitch minimum created at the plasma-vacuum boundary.

The poloidal mode number $m=1$ current-driven kink mode and its resistive MHD counterpart, the tearing mode, are perhaps the most important instabilities in the RFP, and a close-fitting conducting wall is required to provide stability. Tearing modes have been experimentally identified in a number of RFP experiments, and play an important role in MHD models of RFP relaxation and sustainment. Physically the picture is somewhat analogous to the internal disruption in the tokamak. On-axis

heating destabilizes tearing modes with helicity $m=1$ and negative toroidal mode numbers, $n<0$, resonant inside the reversal ($B_\phi=0$) surface. In quasi-steady-state, the modes nonlinearly saturate, and the $\langle\tilde{\mathbf{v}}\times\tilde{\mathbf{B}}\rangle$ fluctuation generated electric field supresses current on-axis and drives poloidal current at the edge. This, in turn, produces a more stable current density profile and toroidal flux; a balance between resistive diffusion and instability is maintained. The end result is an equilbrium closer to the constant-λ BFM.

The location of the conducting wall strongly affects the stability properties of RFP equilibria. If the conducting wall is very close to the plasma, then equilibria which are stable to both kink and tearing modes are possible. For example, BFM equilibria are tearing-mode-stable for $a\lambda<3.12$,[20] quite close to the value of 3.2 at which the helical equilibrium becomes the lowest energy solutions of Eq. 2-1. More realistic equilibria with $J=0$ at the wall can also be stable with a close-fitting conducting wall.[19]

Recently, Ho, Prager, and Schnack, have examined in detail the effect of the RFP boundary condition on the stability of current-driven modes, both linearly[21] and nonlinearly.[22] Their work examines the dependence on the resistive shell time constant and the effect of a large vacuum region. For the linear analysis, they used the MBFM equilibrium shown schematically in Fig. 2-4. The plasma is bounded by a close-fitting resistive shell which may be removed to study independently the effect of the vacuum thickness.

For these equilibria, only $m=0$ and $m=1$ modes were found to be

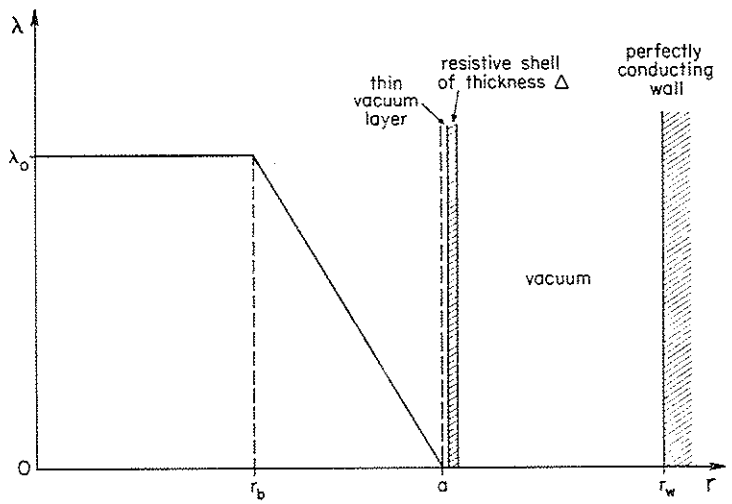

Fig. 2-4. Equilibrium model with MBFM λ profile, resistive shell, vacuum regions and conducting wall (from ref. 21).

unstable. The results for m=1 modes are summarized in Fig. 2-5. The first graph (Fig. 2-5a) shows a stability diagram for the case of a close-fitting conducting shell. The only unstable modes have negative k ($=n/R$), and for typical plasma parameters ($\lambda_o a$<3.4), only the resonant (tearing) modes are unstable. These modes are usually referred to as "dynamo" modes since they are thought to be involved in the RFP sustainment process described above.

The second graph (Fig. 2-5b) shows the results for a vacuum thickness equal to 40% of the plasma radius. Three new regions of instability result. Region II modes are external kinks which are unstable if the total axial flux enclosed by the wall (including the vacuum region),

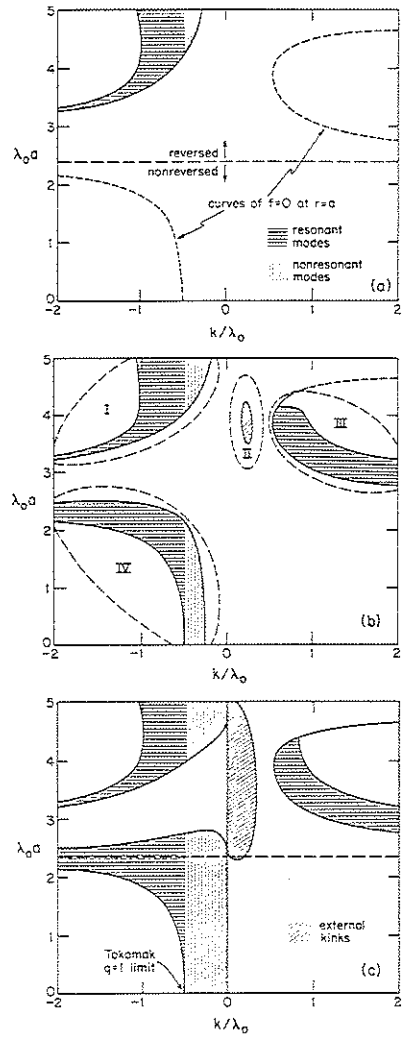

Fig. 2-5. m=1 stability diagrams. Unstable regions are shown shaded for (a) close-fitting conducting wall, (b) 40% vacuum thickness, $[r_w-a]/a$, and (c) 1900% vacuum thickness (effectively no conducting wall). (From ref. 21.)

$$\Phi = \int_0^{r_w} 2\pi r B_\phi \, dr \qquad 2\text{-}4$$

is negative with respect to the sense of the toroidal magnetic field on-axis. The Region III modes are tearing modes resonant outside the reversal surface. Region IV modes are internally resonant and nonresonant modes which occur in nonreversed equilibria, and instability probably results from weak shear, as discussed by Robinson.[18]

When the conducting wall is essentially removed, the results in Fig. 2-5c are obtained. Regions II and IV have grown to the point where no MBFM equilibria are stable to m=1 modes. Without the outer conducting wall, Eq. 2-4 cannot be satisfied for any reversed field equilbrium.

For BFM equilibria, the m=0 mode is stable for $a\lambda$<3.83. If there is *any* vacuum region, though, a sharp λ boundary is extremely destabilizing. The configuration shown in Fig. 2-4 with a very thin vacuum layer is also unstable to m=0 tearing modes, even though λ does not fall abruptly to zero at the edge of the plasma. It is possible, however, to find different, non-constant-λ equilibria which are m=0 stable with small vacuum regions.[19] When the vacuum region is large, the m=0 mode is unstable.

The resistive shell time constant modifies the growth rates of the unstable modes. Those most sensitive are the kink modes and tearing modes resonant in the outer region of the plasma in close proximity to the shell. For these modes, the growth rates increase with a more resistive shell, while the tearing modes resonant internally are less sensitive since they are localized away from the wall.

Using a fully compressible 3-D MHD code, Ho, Prager, and Schnack also studied nonlinear numerical simulations of the configuration in Fig. 2-4. The reference case equilibrium was obtained by running the code with a close-fitting, perfectly conducting wall boundary condition until a sustained quasi-steady-state is reached. As described above, the fluctuation induced electric field, generated primarily by m=1, n<0 modes, supresses toroidal current near the axis and drives poloidal current near the edge. When the vacuum region or shell time is increased, the fluctuation amplitudes and the fluctuation induced electric field increase. Most of the increase is directed to supress current on-axis, and to maintain constant plasma current, the loop voltage must increase. This is illustrated in Fig. 2-6 where the loop voltage required to maintain a given current is plotted as a function of the percentage vacuum thickness. This loop "voltage" is actually the dimensionless quantity

$$V_L = 2\pi \frac{R}{a} \frac{E_o}{\eta J_o}. \qquad 2\text{-}5$$

The "classical" limit is $E_o = \eta J_o$ or V_L=15.7 for the aspect ratio, R/a=2.5, used by Ho, *et. al.* For the close-fitting wall reference equilibrium, the fluctuation-generated electric field is ~30% the resistive contribution. With a 50% vacuum thickness, the fluctuation-generated electric field is ~400% the resistive contribution—more than an order of magnitude increase.

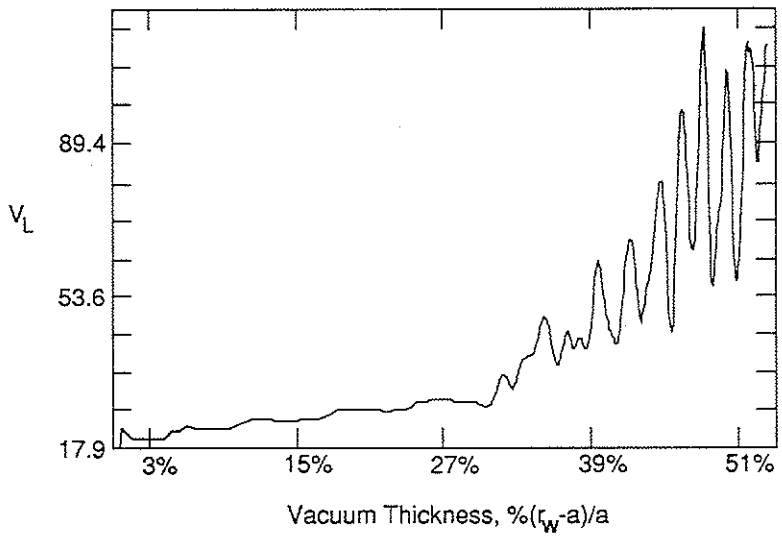

Fig. 2-6. Dimensionless loop voltage, V_L, as a function of vacuum region thickness for constant plasma current. The resistive shell time is 1% of the resistive diffusion time for this case. (From ref. 22.)

REFERENCES

1 H.A.B. Bodin and A.A. Newton, Nucl. Fusion **20**, 1255 (1980).

2 H.A.B. Bodin, Nucl. Instrum. and Methods **207**, 1 (1983).

3 J.B. Taylor, Rev. Mod. Physics **58**, 741 (1986).

4 D.A. Baker and W.E. Quinn, in *Fusion*, edited by E. Teller (Academic, New York, 1981), Vol. 1, Part A, Chap. 7.

5 R. J. La Haye, T. N. Carlstrom, R. R. Goforth, G. L. Jackson, M. J. Schaffer, T. Tamano, and P. L. Taylor, Phys. Fluids **27**, 2576 (1984).

6 H. A. B. Bodin, in *Proceedings of the International Conference on Plasma Physics*, Lausanne, 1984, (EEC, Brussels, 1984), Vol. I, p. 417.

7 V. S. Antoni, S. Martini, S. Ortolani, and R. Paccagnella, in *Mirror Based and Field Reversed Approaches to Magnetic Fusion*, proceedings of the International School of Physics Workshop, [International School of Plasma Physics, Varenna (Como), Italy, 1983], p. 107.

8 S. C. Prager and L. Turner, Phys. Fluids **28**, 1155 (1985).

9 K. F. Schoenberg, R. F. Gribble, and J. A. Phillips, Nucl. Fusion **22**, 1433 (1982).

10 V. D. Shafranov, in *Reviews of Plasma Physics*, (Consultants Bureau, New York, 1965), Vol. II, p. 130.

11 T. G. Cowling, *Magnetohydodynamics* (Hilger, Bristol, England, 1976).

12 See, for example, A. Y. Aydemir, D. C. Barnes, E. J. Caramana, A. A. Mirin, R. A. Nebel, D. D. Schnack, and A. G. Sgro, Phys. Fluids **28**, 898 (1985); H. R. Strauss, Phys. Fluids **27**, 2580 (1984); J. A. Holmes, B. A. Carrerras, T. C. Hender, H. R. Hicks, V. E. Lynch, Z. G. An, and P. H. Diamond, Phys. Fluids **28**, 261 (1985).

13 A. R. Jacobson and R. W. Moses, Phys. Rev. A **29**, 3335 (1984).

14 M. N. Rosenbluth and M. N Bussac, Nucl. Fusion **19**, 489 (1979); W. C. Turner, G. C. Goldenbaum, E. H. A. Granneman, J. H. Hammer, C. W. Hartman, D. S. Pronto, and J. Taska, Phys. Fluids **26**, 1965 (1983).

15 L. Turner, Phys. Fluids **27**, 1677 (1984).

16 R. J. La Haye, T. H. Jensen, P. S. C. Lee, R. W. Moore, and T. Ohkawa, Nucl. Fusion **26**, 255 (1986).

17 J. S. Sarff, J. C. Sprott, and L. Turner, Phys. Fluids **30**, 2155 (1987).

18 D.C. Robinson, Plasma Physics **13**, 439 (1971).

19 D.C. Robinson, Nucl. Fusion **18**, 939 (1978).

20 R. D. Gibson and K. J. Whiteman, Plasma Physics **10**, 1101 (1968).

21 Y. L. Ho and S. C. Prager, Phys. Fluids **31**, 1673 (1988).

22 Y. L. Ho, S. C. Prager, and D. D. Schnack, Nonlinear behavior of the reversed field pinch with nonideal boundary conditions, submitted to Phys. Rev. Letters.

CHAPTER 3

EXPERIMENTAL APPARATUS AND DIAGNOSTICS

The experiments described in this thesis were performed on three devices: Tokapole II, the Wisconsin Levitated Octupole, and the small ring Octupole divertor RFP. All of these internal-ring devices produced four-node, poloidal divertor configurations. A brief description of each device and the principal diagnostics used in this research are the topics of this chapter.

3.1 TOKAPOLE II

Tokapole II[1] is a 44-cm-square cross section, 50-cm major radius toroidal device. Normally, it is operated as a four-node poloidal divertor tokamak, but a modification of the toroidal field circuit allowed the application of a reversed toroidal field for the study of poloidal divertor RFP plasmas.

3.1.1 Machine Description

The Tokapole II aluminum vacuum vessel wall is 3-cm-thick with one insulated gap in each of the toroidal and poloidal directions. In the original design, each of four copper divertor rings were suspended from the vacuum vessel wall by three beryllium copper rods. In a recent

machine upgrade, these beryllium copper rods were replaced by stainless steel rods to allow larger magnetic forces generated by an increase in total divertor ring current. The original total ring current limit was 300 kA, and the upgraded version allows 500 kA. Most of the Tokapole II RFP data reported in this thesis are "pre-upgrade," but some are "post-upgrade." As the data are presented, the version of Tokapole II on which they were obtained will be indicated. Fig. 3-1 shows the relative dimensions and locations of the vacuum tank and divertor rings in a poloidal cross section. Detailed descriptions of the original device are given in references 2 and 3.

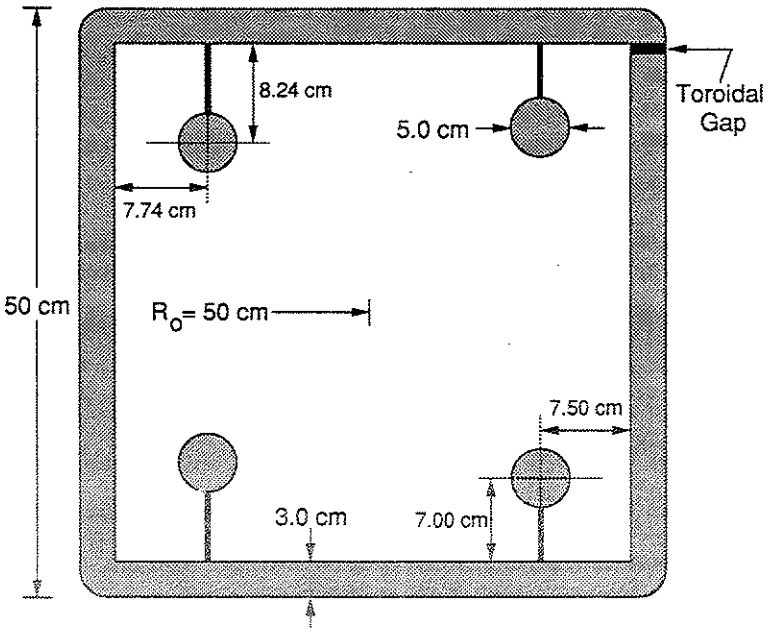

Fig. 3-1. Tokapole II poloidal cross section.

To form the poloidal field, toroidal currents are induced in the rings and plasma by a 40-turn transformer primary winding on an 0.17-Wb iron core (reverse-biased). A 5-kV capacitor bank with maximum stored energy of 90 kJ drives the pulsed poloidal field in the usual "tokamak mode." An additional 10-kV high-voltage startup capacitor bank with maximum stored energy of 15 kJ was installed for optional use in the poloidal divertor "RFP mode."

The toroidal field is generated by solenoidal current in a 4/0 wire wound on the machine in four sections, each with 24 turns. The parallel/series combination of these sections allows a choice of 24:1, 48:1, or 96:1 turns ratios. A 5-kV capacitor bank with maximum stored energy of 650 kJ drives the pulsed toroidal field in the tokamak mode. Only a small fraction of this bank was used in the RFP mode of operation, and the circuit was modified to allow reversed field programming.

A typical equilibrium poloidal flux plot for a tokamak-like equilibrium is shown in Fig. 3-2. The broken contour represents the magnetic separatrix which separates the flux linking a single current—called private flux—from the flux which links all five currents—called common flux. Poloidal divertor RFP equilibria have these same features. Most of the plasma pressure and current is confined within the magnetic separatrix.

Diagnostic access is provided through a number of holes in the vacuum vessel wall. Valve assemblies allow small diameter (~1/4 in) cylindrical probes to be inserted and moved throughout most of the

plasma volume without loss of vacuum. A base vacuum, typically in the low 10^{-7} torr range, is maintained by a 1500-l/sec turbomolecular pump.

3.1.2 Operation as a Poloidal Divertor RFP

Since Tokapole II is normally operated as a poloidal divertor tokamak, some modification of the field programming circuits was required to operate the device as a poloidal divertor RFP. The electrical circuits used in the RFP mode of operation are shown in Fig. 3-3.

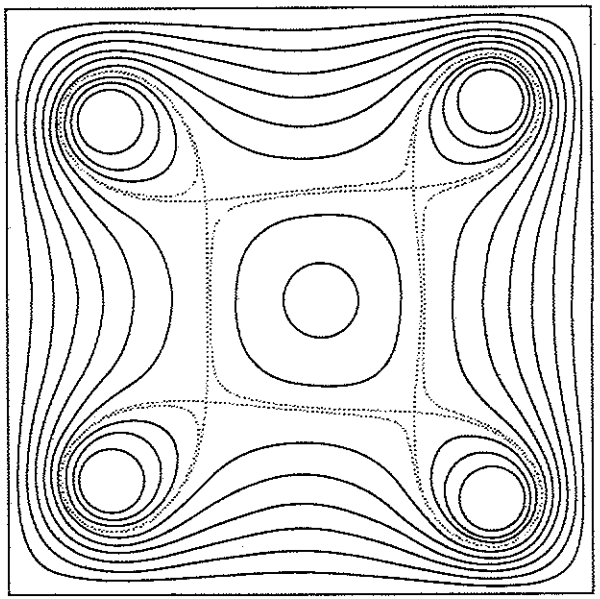

Fig. 3-2. Typical theoretical equilibrium poloidal flux plot for a Tokapole II poloidal divertor tokamak plasma.

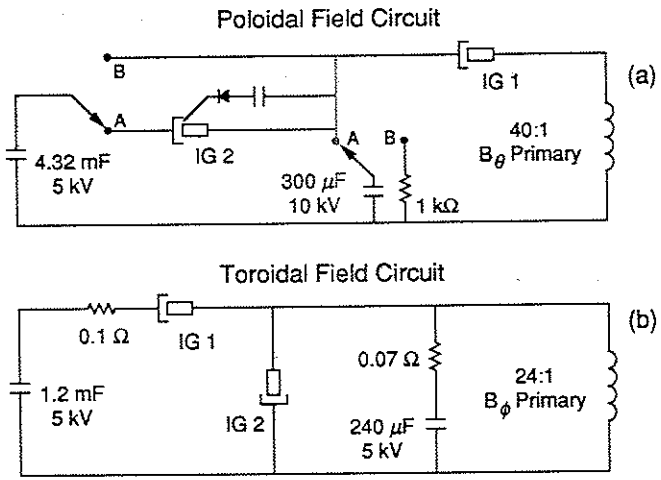

Fig. 3-3. The (a) poloidal and (b) toroidal magnetic field producing circuits in the RFP mode of operation on Tokapole II.

In the poloidal field circuit (Fig. 3-3a), two capacitor banks were available: the usual 5-kV tokamak bank and a 10-kV high-voltage startup bank. With the high-voltage bank installed, the switches were in the "A" positions, and poloidal gap voltages ≤200 V were obtained. If only the 5-kV bank was used, the switches were in the "B" positions, and the gap voltage was limited to ≤100 V. Because the resistance of the RFP was large, RFP operation was optimized for maximum poloidal gap voltage, and the capacitor banks were always fully charged. The number of 5-kV capacitors was chosen to not exceed the total ring current limit at full-volts; if the high-voltage bank was used, fewer 5-kV capacitors were needed. The main

ignitron switch (IG 1) was closed first. When the high-voltage startup bank was used, the 5-kV bank served as a power "crowbar," and the crowbar ignitron (IG 2) was self-triggered when the voltage across the startup bank reached ~5 kV.

The toroidal field circuit is shown in Fig. 3-3b. The four quadrants of the winding were connected in parallel (24:1) to produce the minimum inductance configuration for fast programming. Five 240-μF, 5-kV capacitors formed the main bank. This capacitance was the minimum required to produce toroidal field strengths sufficient for 2.45-GHz electron cyclotron microwave preionization. A single 240-μF, 5-kV capacitor connected across the toroidal field winding formed an under-damped R-L-C circuit allowing the winding current (and, therefore, the toroidal field at the wall) to reverse direction when the main ignitron (IG 1) stopped conducting (*i.e.*, when the winding current approached zero). A second ignitron (IG 2) passively crowbarred the winding current at a specified time after reversal. The two resistors, 0.1 Ω and 0.07 Ω, protected the ignitrons under fault conditions.

The timing sequence and typical waveforms for initiating an RFP discharge on Tokapole II are shown in Fig. 3-4. Several seconds before the discharge was initiated, a 100-W, cw 2.45-GHz microwave source was switched on. The vacuum vessel was filled with hydrogen through a fast piezoelectric valve before the start of the toroidal field. The poloidal field started at or slightly after the peak of the toroidal field. After the toroidal field at the wall (winding current) was reversed, the passive crowbar

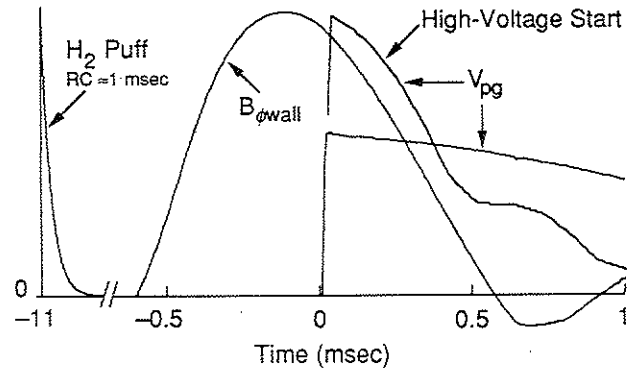

Fig. 3-4. Timing sequence for the initiation of a poloidal divertor RFP plasma in Tokapole II.

ignitron in the toroidal field circuit was triggered. This ignitron would usually stop conducting ~200 μsec later, but this proved irrelevant since RFP-like equilibria did not endure that length of time.

3.2 OCTUPOLE DIVERTOR RFP CONFIGURATIONS

Two, four-node poloidal divertor configurations were examined using the vacuum vessel and hardware of the Wisconsin Levitated Octupole.[4] The first attempt was made in the original device. Unlike past experiments in which plasma was injected into the ring-current-generated octupole magnetic field, a poloidal divertor configuration was formed by inducing current in the rings *and* plasma, as in Tokapole II. A second

attempt was made after smaller rings were placed in the device; the smaller rings increased the ratio of plasma current to ring current.

3.2.1 Levitated Octupole Divertor RFP

The Octupole dimensions were relatively large; the major radius was 1.39 m, and the average minor radius was 0.56 m. The noncircular vacuum vessel was designed to allow removal of the ring supports during the multipole experiment, *i.e.*, the rings were magnetically levitated. The protrusions on the midplane, known as the "noses," created nearly force-free positions in the vicinity of the rings for this purpose. For the experiments described in this thesis, the ring supports were not removed. Single insulated cuts in each of the poloidal and toroidal directions allowed prompt field penetration. A cross section of the device is shown in Fig. 3-5. Detailed descriptions of the device and its operation as a multipole can be found elsewhere.[5]

The poloidal field was generated in the Octupole the same way as in Tokapole. A 38-turn transformer primary winding on a 1.9-Wb iron core (reversed-biased) was connected to a 600-kJ, 5-kV capacitor bank. No high-voltage startup bank was employed on this device. A theoretical poloidal magnetic flux plot for a four-node poloidal divertor RFP plasma is shown in Fig. 3-6.

The toroidal field was produced by wall current fed from 44 pairs of leads connected across the toroidal insulated gap and uniformly distributed

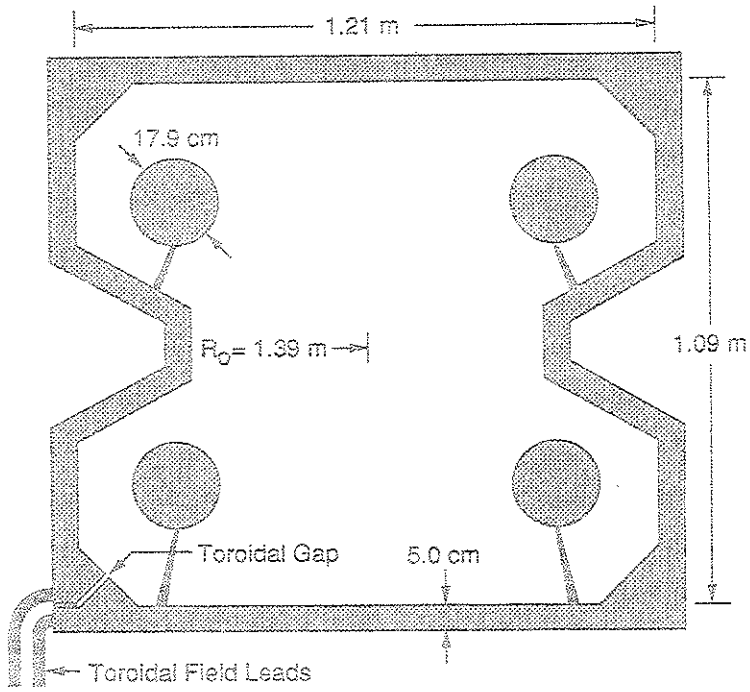

Fig. 3-5. Levitated Octupole poloidal cross section.

in the toroidal direction (see Fig. 3-5). The other ends of each pair were connected to a single-turn transformer secondary winding on a 0.15-Wb iron core. The transformer primary was a pair of 20-turn windings that could be connected in either a 20:1 or 40:1 turns ratio; usually the 20:1 ratio was used.

The toroidal field electrical circuit is shown in Fig. 3-7. Instead of forming an R-L-C circuit to obtain field reversal (as for Tokapole II), a

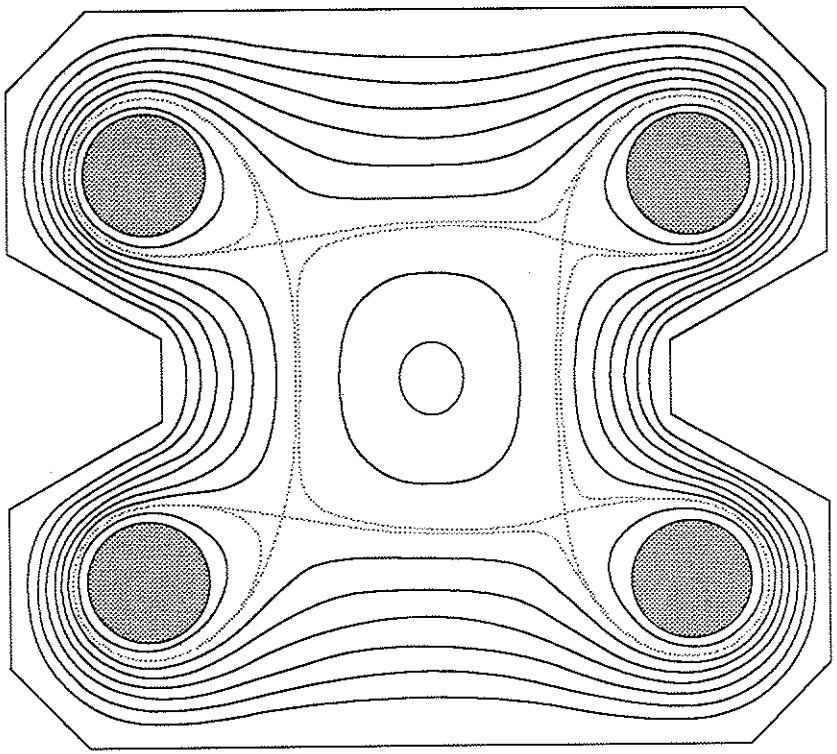

Fig. 3-6. Typical theoretical equilibrium poloidal magnetic flux plot for a poloidal divertor RFP plasma in the Levitated Octupole. The plasma current is 12% of the total ring current.

second ignitron (IG 2) was connected with opposite polarity across the main ignitron (IG 1) and self-triggered when the primary current approached zero. The passive crowbar ignitron (IG 3) was triggered when the desired negative current was obtained. The fourth ignitron (IG 4) was

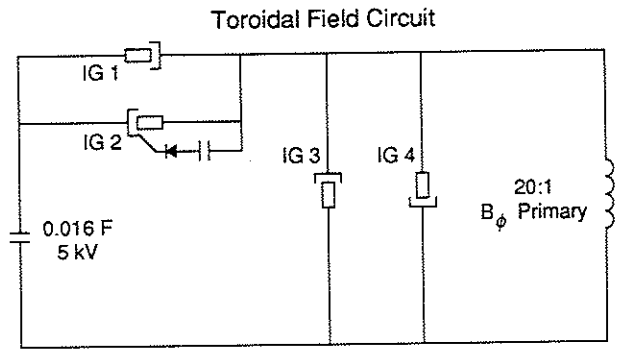

Fig. 3-7. Toroidal magnetic field producing circuit for the RFP mode of operation on the Octupole.

analogous to IG 2, although it was not self-triggered and could not be reliably started.

The initiation of a Levitated Octupole divertor RFP discharge followed the same sequence as described in Fig. 3-4, but the timescale was longer. The time from peak toroidal field—also the start of the poloidal field—to the reversal of the toroidal field at the wall was ~3 msec. A 50-W, cw 2.45-GHz microwave source provided ECRH preionization.

Diagnostic access was provided through valved holes in the vacuum vessel wall. A base vacuum in the low 10^{-8} torr range was maintained by two turbomolecular pumps (1100-l/sec total pumping speed), a cryogenic panel, and six titanium getters.

3.2.2 Small Ring Octupole Divertor RFP

The poloidal gap insulation on the Levitated Octupole was insufficient to prevent arcing for gap voltages ~100 V. To facilitate the development of a suitable gap protection scheme, the poloidal divertor experiments were suspended, and the divertor rings were removed. A successful gap protector was developed during the operation of a large, noncircular RFP in the Octupole tank without rings.[6] This gap protector consisted of 6-mm-thick Viton extending 1 cm into the plasma region and was covered on the top and sides by high-density polyethylene fixtures. Overall was a ceramic shield. The total radial height and toroidal extent of the protector were 2.5 cm and 20 cm respectively. No arcs occurred for typical gap voltages of 200–300 V.

A return to the poloidal divertor RFP experiment began with the installation of four new 2219-T8 aluminum divertor rings. The poloidal cross section of the device is shown in Fig. 3-8. The rings were positioned near the force-free locations generated by the "noses" and were rigidly strapped to pairs of 6.35-mm-diameter Inconel rods attached to the vacuum vessel wall at six (inner rings) or eight (outer rings) toroidal azimuths. The vertical positions of the rings were chosen to minimize the magnetic forces (in the absence of plasma current) measured by accelerometers attached to the rings. The resulting positions were not quite up-down symmetric as indicated by the vertical (y) ring position measurements in Table 3-1. The ~1-cm discrepancy in the horizontal (x) placement of the outer rings was

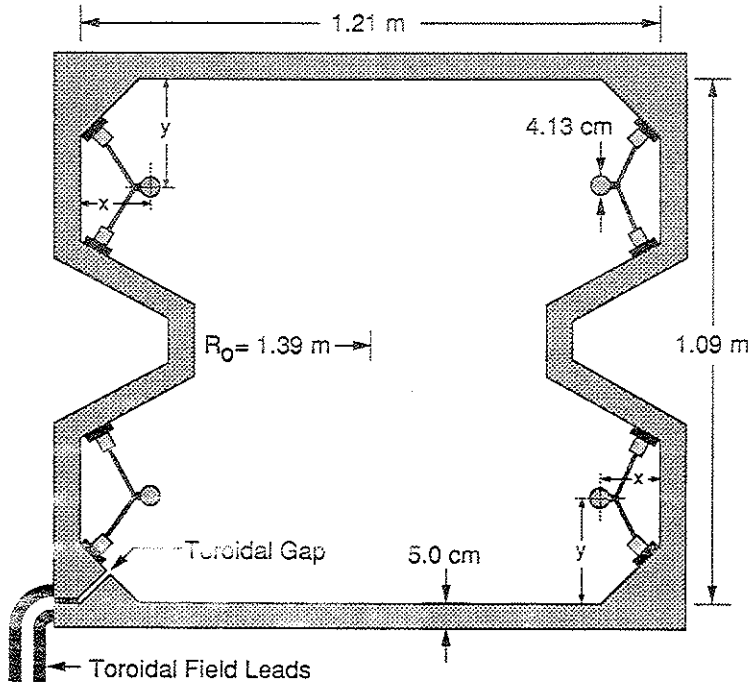

Fig. 3-8. Small ring Octupole poloidal cross section.

due to a distortion in the vacuum vessel.[7] The asymmetric ring placement assured safe operation up to a total ring current of 500 kA. This procedure for ring placement, in effect, measured the device symmetry; therefore, symmetric placement of the rings would not have prescribed symmetry.

The poloidal and toroidal fields were produced using the hardware of the Levitated Octupole, although the poloidal field primary winding was modified to allow 12:1 and 8:1 turns ratios (the 12:1 ratio was most often

Table 3-1: Ring Positions

Ring	*x (cm)*§	*y (cm)*§
upper outer	12.8±0.1	22.8±0.1
lower outer	11.9	21.7
upper inner	14.4	22.0
lower inner	14.5	23.4

§*x and y refer to Fig. 3-8*

used). Also, a 430-μH inductor was placed in series with the primary to provide current limitation in the event of a poloidal gap arc. (No arc was observed.) A theoretical equilibrium poloidal magnetic flux plot for a four-node, poloidal divertor RFP in the Octupole with small rings is shown in Fig. 3-9.

Discharge formation was similar to the methods used on the Levitated Octupole and Tokapole II, but a stronger, 2-kW, 2.45-GHz microwave source was available for these experiments. The base vacuum pressure was typically in the mid 10^{-7} torr range.

3.3 DIAGNOSTICS

In this section, the diagnostics used routinely to measure the global plasma parameters, *e.g.*, plasma current, ring current, toroidal field, density, *etc.*..., are described. Also described are the probes used to measure the local properties of the magnetic field.

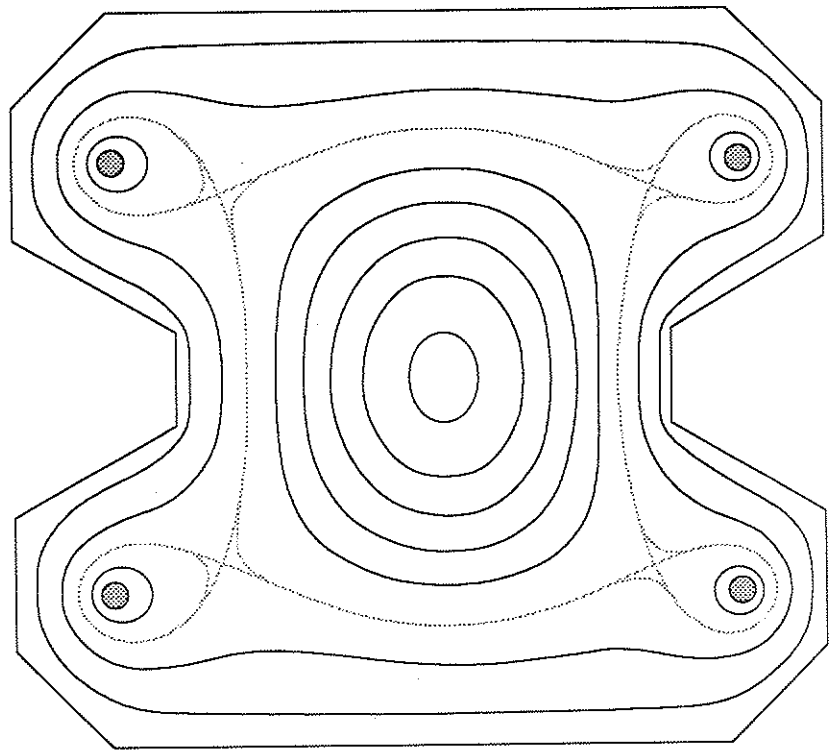

Fig. 3-9. Typical theoretical equilibrium poloidal magnetic flux plot for a poloidal divertor RFP plasma in the small ring Octupole. The plasma current is 60% of the total ring current.

3.3.1 General Diagnostics

Measurement of the toroidal plasma current in the four-node poloidal divertor configuration is difficult, but measurement of the *total* secondary current, *i.e.*, the sum of the plasma current and ring currents, is not. For example, early in time the poloidal field primary current is related to the secondary current by the transformer turns ratio. Late in time, though, magnetizing currents become large as the iron saturates. A more direct measurement of the total secondary current may be obtained unobtrusively using a Rogowski coil located near the vacuum vessel wall. Unfortunately, attempts to measure the ring current routinely by mounting close-fitting Rogowski coils on the rings have failed in the harsh plasma environment.

The sum of the ring and plasma currents can be separated into the two components using a simple circuit model.[8] If the iron core has infinite permeability and the rings are perfectly conducting, then the rate of change of the total flux linking the rings may be written

$$\dot{\Phi}_c + \dot{\Phi}_r + \dot{\Phi}_{rp} = 0 \qquad 3\text{-}1$$

where Φ_c is the core flux, Φ_r is the ring-generated-flux, and Φ_{rp} is the plasma-generated-flux which links the rings. Substituting $\dot{\Phi}_c = V_{pg}$, $\dot{\Phi}_r = -L_r \dot{I}_r$, and $\dot{\Phi}_{rp} = -M\dot{I}_p$ where V_{pg} is the poloidal gap voltage, L_r is the total ring inductance, M is the mutual inductance between the plasma and

ring currents, I_r is the total ring current, and I_p is the plasma current, Eq. 3-1 may be solved for I_r:

$$I_r = \frac{1}{L_r}\int V_{pg}\,dt - \frac{M}{L_r} I_p \ . \qquad 3\text{-}2$$

The plasma current is given by

$$I_p = I_t - I_r \qquad 3\text{-}3$$

where I_t is the total secondary current measured by a Rogowski coil or the primary current.

From calculations of the vacuum field, the ratio α, of poloidal flux linking all four rings to the total poloidal flux may be determined. If the plasma current is a filament on axis, then it links only this common flux, *i.e.*, $\Phi_{pr} = \alpha L_r I_r = M I_r$ where Φ_{pr} is the ring flux that links the plasma. The ratio $M/L_r = \alpha$.

For each device, an analog computer was constructed to perform the calculations of Eqs. 3-2 and 3-3. The common flux ratio was 0.5, 0.8, and 0.127 for Tokapole II, the Levitated Octupole, and the small ring Octupole devices respectively. In reality, the plasma is diffuse and finite ring resistance allows current soak-in; L_r becomes time dependent, and flux is lost resistively. The current soak-in effects were estimated using an idealized calculation of a uniform field soaking into a long cylindrical conductor[9] and were incorporated into the computer circuitry.

The details of the magnetic topology in the four-node poloidal divertor depend on the relative magnitudes of the ring and plasma currents. Since the region within the separatrix is of most interest, an estimate of its volume, or equivalently its poloidal cross-sectional area, is useful for determining the size of the plasma. For the case of five filamentary currents, four equal to $I_r/4$ located on the corners of a square and the fifth equal to I_p located at the center, it is easy to show that the distance to the "x-point" poloidal field nulls on the diagonals of the square is given by

$$d_{x\text{-}pt} = d\,[I_p/(I_p + I_r)]^{1/4} \qquad 3\text{-}4$$

where $2d$ is the square diagonal length. These "x-points" roughly define the boundary and cross-sectional area of the nearly square separatrix. This idealized calculation indicates how the area within the separatrix should scale with the ratio I_p/I_r. Using theoretical equilibrium flux plots to determine more exactly the area enclosed by the separatrix, this scaling was shown to be accurate.[10] For Tokapole II plasmas, the area enclosed by the separatrix is given by

$$A_{sep} = 299\,[I_p/(I_p + I_r)]^{1/2}\ \text{cm}^2. \qquad 3\text{-}5$$

For the small ring Octupole plasmas,

$$A_{sep} = 0.63\,[I_p/(I_p + I_r)]^{1/2}\ \text{m}^2. \qquad 3\text{-}6$$

The average toroidal field, defined as the total toroidal flux enclosed within the vacuum vessel, Φ, divided by the poloidal cross-sectional area,

$$\langle B_\phi \rangle = \Phi / Area\ , \qquad 3\text{-}7$$

was measured by integrating a flux loop at the wall. For Tokapole II and the Levitated Octupole, this loop was the vacuum vessel itself.

Since the vacuum vessel has a toroidal gap, the average toroidal field at the wall is obtainable from Ampere's law applied along a line of constant major radius, R_{wall}, and is proportional to the winding current, $I_{\theta w}$ (assuming axisymmetry):

$$\langle B_{\phi wall} \rangle = \mu_o I_{\theta w}/2\pi R_{wall}\ . \qquad 3\text{-}8$$

The winding current was measured by a Rogowski coil for these studies.

The midcylinder chord-averaged electron density was measured by either a 70-GHz or a 140-GHz microwave interferometer. Unfortunately, this diagnostic was unreliable most of the time on all of the devices. The few times when it was somewhat functional, at least an indication of the magnitude of the central plasma density was obtained.

Most of the data reported in this thesis were acquired using 10-bit, bipolar (±5V) digitizers at a sampling rate of 1 MHz. The general diagnostics were usually sampled at 100 kHz. The data were handled and stored by a Digital Equipment Corporation Micro VAX II computer. The "pre-upgrade" Tokapole II and Levitated Octupole data were obtained on a

Tektronix Model 466, 20-MHz oscilloscope and were recorded on Polaroid photographs.

3.3.2 Magnetic Probes and Analog Integrators

The magnetic field within the plasma was measured with small movable magnetic probes. These probes consisted of coils of wire placed inside vacuum-sealed cylindrical tubes. The coils were wound on forms and were mounted with their axes either perpendicular ("transverse") or parallel ("radial") to the axis of the tube. The probes were usually aligned with their axes perpendicular to the vacuum vessel so that "transverse" corresponds to "poloidal" or "toroidal." Some probes had three orthogonal coils wound on one form to measure simultaneously all components of the magnetic field at the same location, while others were just a single coil.

The cross section of a typical probe assembly is shown in Fig. 3-10. A 0.13-mm-wall stainless steel tube, plugged on one end, was soldered to a 6.35-mm-diameter thick-walled stainless steel tube. The thin-walled tube, which provided electrostatic shielding for the coils inside, was protected from the plasma by a boron nitride sheath cemented to its surface. The 6.35-mm tube was polished to form a vacuum O-ring surface allowing the probe assembly to be moved without loss of vacuum. Profiles of the magnetic field could be obtained this way.

If the probe dimensions are small compared to the magnetic field gradients, then the coil output is proportional to the locally changing field

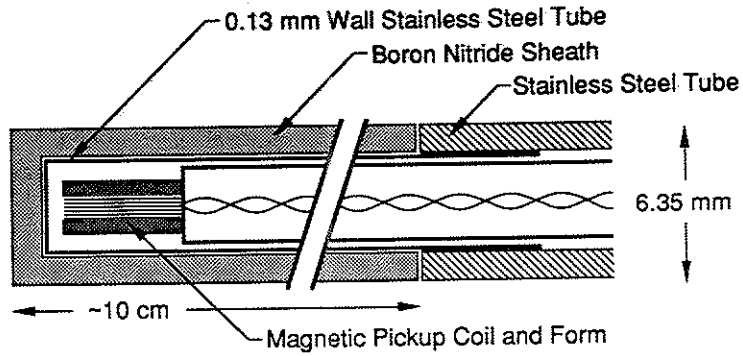

Fig. 3-10. Cross sectional view of a typical magnetic probe assembly.

strength. To obtain the local magnetic field, the coil output was time-integrated using the active circuit shown in Fig. 3-11. The integration bandwidth for this circuit is 0.0016 Hz–700 kHz, and the effective integration time constant is variable over the range 1–100 μsec. An auto-zeroing feature maintains an input offset voltage between the integrating amplifier inputs less than 0.5 μV, effectively eliminating integrator drift errors. The output is switchable between the integral and the zero-field reference voltage. This allowed high speed digitization of the toroidal field which was sometimes programmed to start long before the poloidal field. There is also a buffered input for monitoring the coil signal without disturbing the integration.

For the equilibrium profile studies on Tokapole II (Chapter 4, section 4.2.1), the circuit in Fig. 3-11 was not yet available. The integrator circuit in

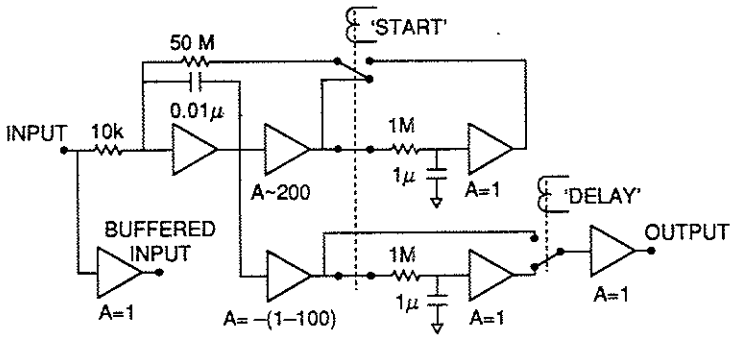

Fig. 3-11. Active integrator circuit with auto-zeroing and reference-voltage memory features.

Fig. 3-12 was used for these measurements. The integration bandwidth for this circuit is 0.16 Hz–5 kHz, and the integration time constant is 100 μsec. A narrow bandwidth was chosen because the signals were measured using an oscilloscope, and the data were recorded on Polaroid photographs. A more readable trace was obtained if the high frequency magnetic fluctuations were low-pass filtered.

The coil sensitivity was calibrated in a known magnetic field (generated by a Helmholtz coil) at a variety of frequencies less than 100 kHz. The 0.13-mm wall stainless steel electrostatic shield attenuates the magnetic field at frequencies higher than this. The coil response was linear to within a few percent for frequencies up to 100 kHz, *i.e.*, the –3-dB bandwidth of a shielded coil was ~400 kHz.

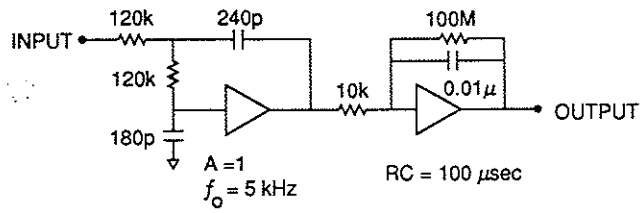

Fig. 3-12. Active integrator circuit used for the equilibrium magnetic field measurements on Tokapole II.

REFERENCES

1 A. P. Biddle, R. N. Dexter, R. J. Groebner, D. J. Holly, B. Lipschultz, M. W. Phillips, S. C. Prager, and J. C. Sprott, Nucl. Fusion 19, 1509 (1979).

2 J. C. Sprott and T. W. Lovell, University of Wisconsin-Madison PLP 744 (1978).

3 R. J. Groebner, Ph.D. Thesis, University of Wisconsin-Madison (1979).

4 D. W. Kerst, H. K. Forsen, D. M. Meade, D. E. Lencioni, J. C. Sprott, H. V. De la Fuente, A. W. Molvik, R. A. Breun, A. J. Cavallo, J. R. Drake, J. R. Greenwood, T. C. Jernigan, R. Prater, and J. W. Rudmin, in *Plasma Physics and Controlled Nuclear Fusion Research*, 1971, Proceedings of the 4th International Conference, Madison (IAEA, Vienna, 1972), Vol. 1, p. 3.

5 See J. D. Steben, J. Appl. Phys. 43, 1211 (1972); J. R. Drake, Ph.D. Thesis, University of Wisconsin-Madison (1974); A. J. Cavallo, Ph.D. Thesis, University of Wisconsin-Madison (1975); C. J. Armentrout, Ph.D. Thesis, University of Wisconsin-Madison (1977).

6 A. Almagri, S. Assadi, R. N. Dexter, S. C. Prager, J. S. Sarff, and J. C. Sprott, Nucl. Fusion 11, 1795 (1987).

7 E. J. Strait and C. J. Armentrout, University of Wisconsin-Madison PLP 801 (1979).

8 J. C. Sprott, University of Wisconsin-Madison PLP 889 (1983); S. C. Prager, J. C. Sprott, T. H. Osborne, and K. Miller, University of Wisconsin-Madison PLP 756 (1978).

9 D. W. Kerst and J. C. Sprott, J. Appl. Phys. 60, 475 (1986).

10 J. S. Sarff, University of Wisconsin-Madison PLP 1003 (1987).

CHAPTER 4

EXPERIMENTAL RESULTS

The results of the experimental attempts to form four-node poloidal divertor RFP plasmas in Tokapole II, the Levitated Octupole, and the small ring Octupole are presented in this chapter. Measurements of the equilibrium magnetic field profiles in Tokapole II plasmas are presented first to illustrate the features of the four-node poloidal divertor configuration. These discharges exhibited transient RFP-like equilibria, and the magnetic separatrix was observed to limit both the plasma current and pressure. An interesting feature of the discharges was a large diamagnetic current resulting from the sharp drop in the plasma pressure near the separatrix.

In the Levitated Octupole, only preliminary data were obtained before the removal of the rings was required to develop a poloidal gap protection scheme. Qualitatively the discharges were similar to the transient RFP-like plasmas in Tokapole II.

The results from the small ring Octupole device were, at first, encouraging. Measurements of the plasma current, average toroidal field, and the toroidal field at the wall indicated nearly steady-state RFP-like equilibria for ~1 msec. Local measurements of the magnetic field, however, uncovered a large, stationary, asymmetric component which set in about the time when the spatially averaged toroidal field reversed at the wall.

This stationary asymmetry was not observed in the Tokapole II plasmas. Since the profile measurements ("pre-upgrade") would not have identified such behavior, the experiment was repeated ("post-upgrade") to look explicitly for asymmetries. Nothing resembling that in the small ring Octupole plasma was observed. A concern in the small ring Octupole experiment was that large field errors at both the poloidal and toroidal gaps might have caused the asymmetry. If this were the case, then the errors in Tokapole II might have been too small to initiate similar asymmetry. To test this hypothesis, the Tokapole II primary winding was modified to enhance the poloidal gap field error, but again, no asymmetry like that in the small ring Octupole plasma was observed.

4.1 TOKAPOLE II RESULTS

4.1.1 Equilibrium Properties

The time evolution of the basic electrical quantities for a typical poloidal divertor RFP discharge in Tokapole II is shown in Fig. 4-1. This discharge was obtained without the high voltage startup bank in the "post-upgrade" version of Tokapole II. The broken-curve plot of the toroidal plasma current is actually a local measurement of the midplane poloidal field near the wall. The circuit model (described in section 3.3.1) overestimates the current early in time as it diffuses into the plasma,[1] so the local measurement probably more accurately represents the time

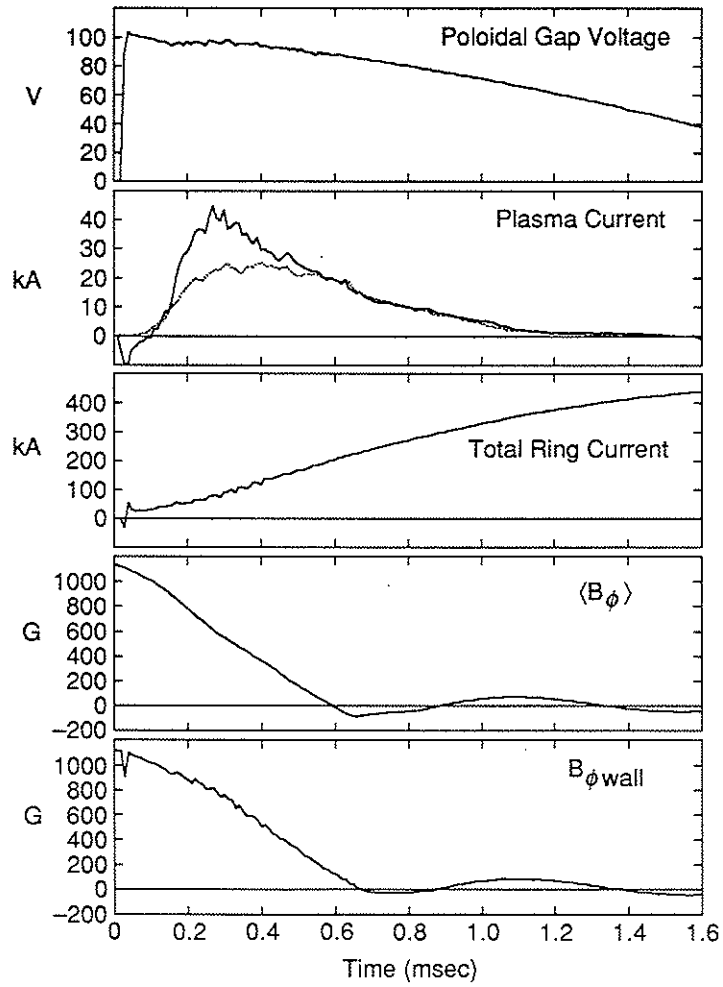

Fig. 4-1. Time evolution of the basic electrical quantities for a typical poloidal divertor RFP discharge in Tokapole II (post-upgrade).

evolution of the plasma current. (A local measurement is exact if the current density is cylindrically symmetric.) The time evolution of the poloidal gap voltage, plasma current, and average toroidal field for a "pre-upgrade" discharge using the high voltage startup bank is shown in Fig. 4-2. The waveforms in Fig. 4-2 are smooth because they were "hand-digitized" from photographs of oscilloscope traces. The photographs show small fluctuations like those in the waveforms in Fig. 4-1.

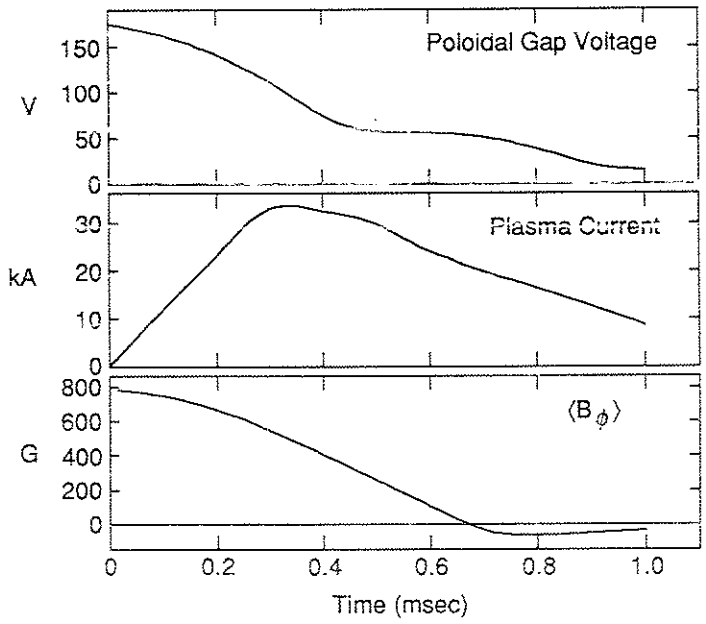

Fig. 4-2. Time evolution of the basic electrical quantities for a typical poloidal divertor RFP discharge in Tokapole II using the high-voltage start bank (pre-upgrade).

If the poloidal field was initiated earlier in the toroidal field waveform, a larger peak plasma current could be obtained, but at the time the toroidal field reversed at the wall, it was about the same. If the poloidal field was initiated more than ~100 μsec later than shown in Figs. 4-1 or 4-2, a smaller plasma current was obtained at all times. Degradation was also observed if the toroidal field was too small to allow ECRH preionization, or if the hydrogen fill pressure was below ~2 mtorr (measured by a fast ion gauge).

Internal measurements of the magnetic field were obtained using magnetic probes. The perturbational effect of the probe is illustrated in Fig. 4-3 which shows a comparison of the plasma current waveforms for an unperturbed plasma and a plasma with a magnetic probe inserted to the axis. The length of the discharge was slightly shortened, but the early time behavior was similar. This perturbation of the plasma current was observed only if the tip of the probe was near the center of the plasma (within the separatrix).

For RFP-like equilibria, the toroidal field on axis must have the opposite polarity as the toroidal field at the wall. Fig. 4-4 shows the toroidal field measured by a magnetic probe located 3 cm from the geometric axis on the midplane and the toroidal field at the wall, *i.e.*, the toroidal field winding current. The toroidal field at the center of the plasma fell throughout the discharge, but more slowly than at the wall. Transient reversed field equilibria were obtained for ~100 μsec. Profiles of the midplane magnetic field were obtained by moving the magnetic probe in

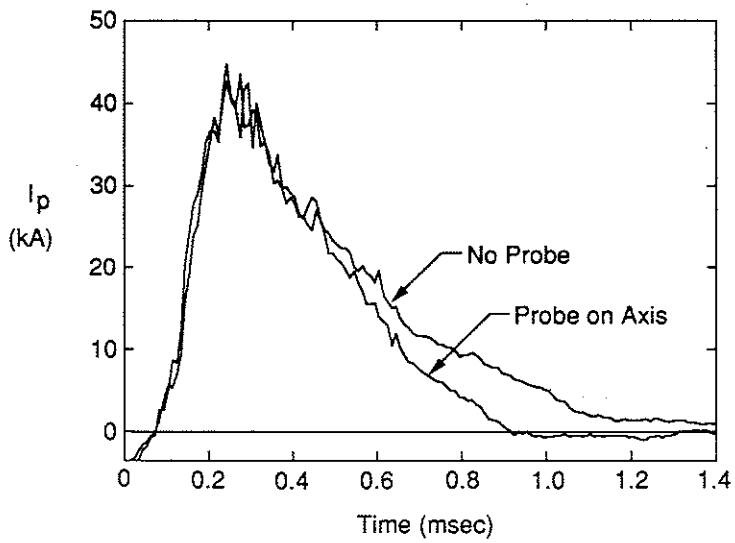

Fig. 4-3. Comparison of the plasma current with and without a magnetic probe on-axis (post-ugrade).

1 cm increments and taking several shots at each location for averaging the shot-to-shot irregularities. Fig. 4-5 shows exemplary data obtained at a time when the toroidal field at the wall was slightly reversed. The error bars indicate the statistical accuracy of the shot-to-shot reproducibility. Least-square cubic spline polynomials fit to the data provided an analytic representation of the equilibrium magnetic field from which the current density was calculated. The time evolution of the magnetic field profiles is illustrated in Fig. 4-6 by plotting the polynomials at 20 μsec intervals. The decay illustrated in Fig. 4-4 is apparent in Fig. 4-6a.

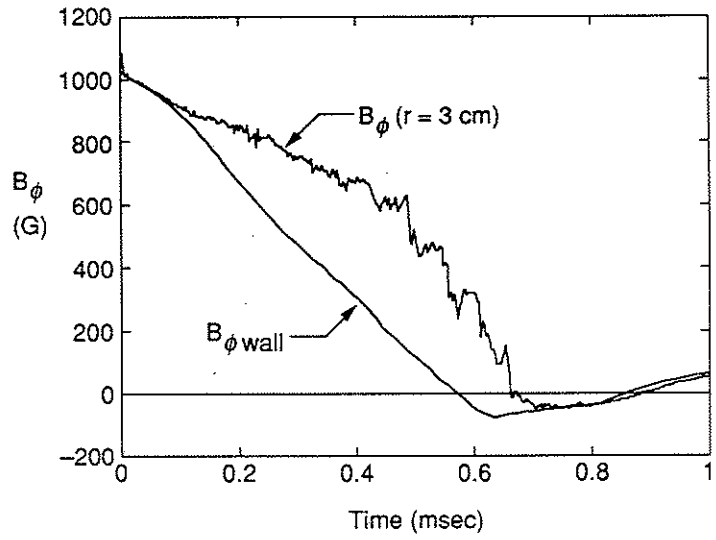

Fig. 4-4. Time evolution of the axis toroidal field and the toroidal field at the wall, *i.e.*, the winding current (post-upgrade).

The plasma current density was obtained using Ampere's law, $\nabla\times\mathbf{B}=\mu_o\mathbf{J}$ (neglecting displacement current). Assuming toroidal axisymmetry, the equations for the poloidal and toroidal components of the current density on the midplane in the toroidal coordinate system r,θ, and ϕ are respectively

$$\mu_o J_\theta = \frac{1}{R}\frac{\partial}{\partial r}(RB_\phi) \qquad 4\text{-}2$$

and

$$\mu_o J_\phi = \frac{1}{r}\frac{\partial}{\partial r}(rB_\theta) - \frac{1}{r}\frac{\partial B_r}{\partial \theta} \qquad 4\text{-}3$$

where $R = R_o + r\cos\theta$ is the major radius. The θ-derivative in Eq. 4-3 is large in the four-node poloidal divertor geometry, but most of the noncircularity is associated with the ring-generated field. If the plasma current is assumed to be cylindrically symmetric about the magnetic axis, then radial field is generated only by the rings. The equation for the toroidal current density

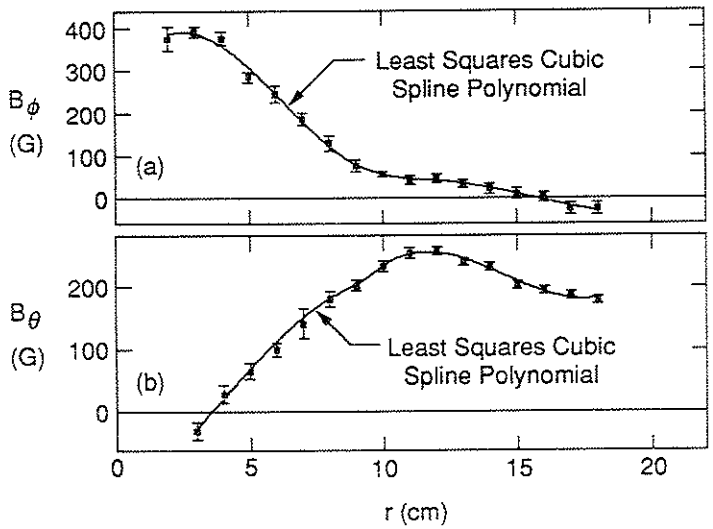

Fig. 4-5. Typical radial profiles of the (a) toroidal and (b) poloidal ($B_\theta - B_{\theta vac}$) components of the midplane magnetic field (pre-upgrade).

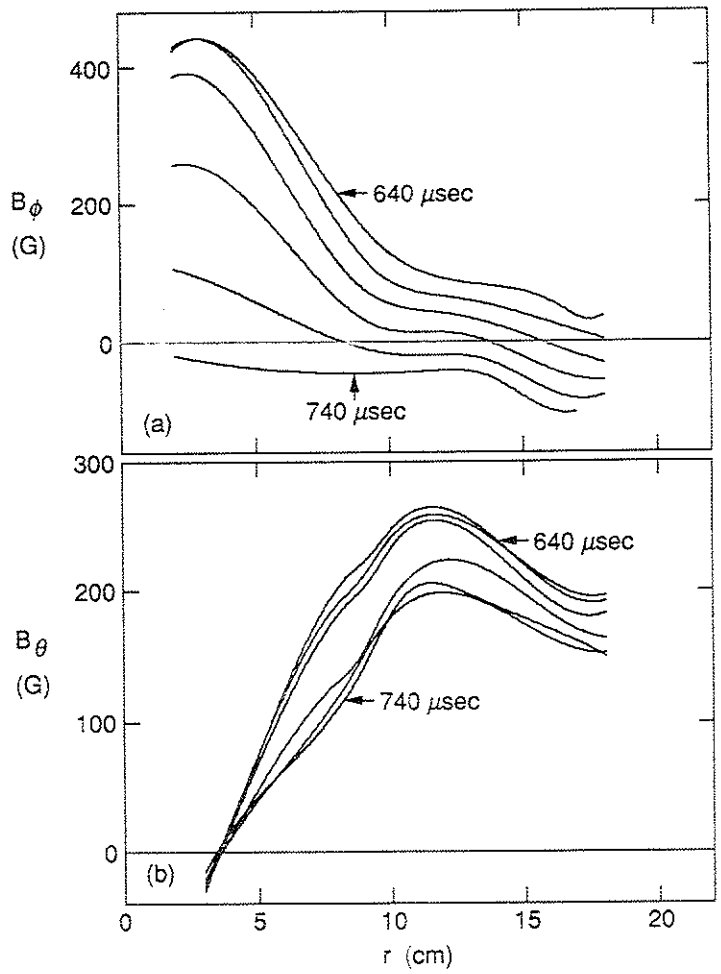

Fig. 4-6. Cubic spline polynomial representations of the radial profiles of the midplane magnetic field: (a) toroidal and (b) poloidal ($B_\theta - B_{\theta vac}$). The polynomials are plotted in 20 μsec intervals.

then becomes

$$\mu_o J_\phi = \frac{1}{r}\frac{\partial}{\partial r}[r(B_\theta - B_{\theta vac})] \qquad 4\text{-}4$$

where $B_{\theta vac}$ is the poloidal field measured in vacuum. (Eq. 4-4 implicitly assumes the ring current distribution is the same with and without plasma; in Tokapole II, the mutual coupling of the rings and the plasma is weak.) The assumption of cylindrical symmetry overestimates the toroidal current density near the separatrix. For example, if the toroidal current density is constant within the separatrix and zero outside, then Eq. 4-4 errs near the separatrix by ~20%. For more realistic profiles, *e.g.*, parabolic, Eq. 4-4 errs near the separatrix by only ~8% of the magnetic axis value.

The profiles of the toroidal and poloidal current density obtained from the polynomials fit to the data in Fig. 4-5 are shown in Fig. 4-7, and the $\lambda_{||} = \mu_o \mathbf{J}\cdot\mathbf{B}/B^2$ and $\lambda_\perp = -\mu_o \mathbf{J}\times\mathbf{B}\cdot\hat{\mathbf{r}}/B^2$ profiles are shown in Fig. 4-8. (The error bars reflect only the statistical uncertainty of the magnetic field data.) As expected, $\lambda_{||}$ is not constant with radius but falls sharply near r=10 cm where the separatrix crosses the midplane. The peak in $\lambda_\perp$ near the separatrix identifies a large diamagnetic (perpendicular) current and concomitant gradient in the plasma pressure. By integrating the force balance equation, $\nabla p = \mathbf{J}\times\mathbf{B}$, the pressure profile in Fig. 4-9 was obtained. The magnetic pressure, $B^2/2\mu_o$, is also shown to illustrate that the central $\beta = 2\mu_o p/B^2$ value was order unity. This large beta probably resulted, in part, from the good confinement of the octupole component of the

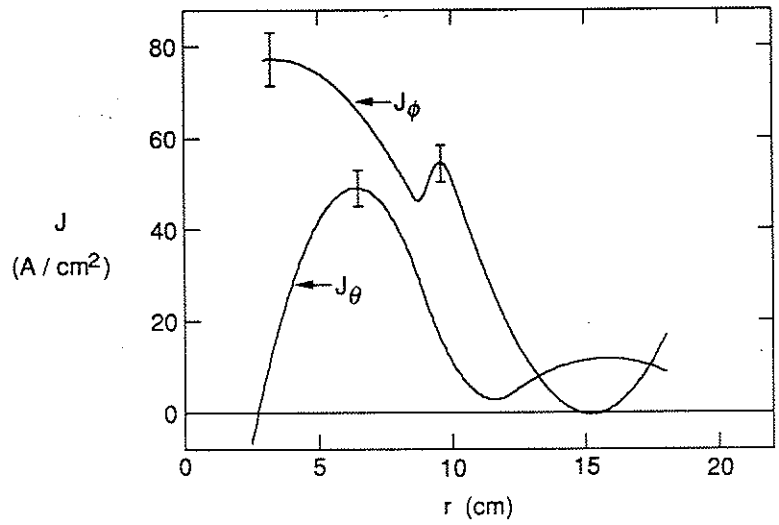

Fig. 4-7. Radial profiles of the midplane current density derived from the data in Fig. 4-5.

magnetic field which dominates in the common flux region. Independent measurements of the plasma temperature and density were not accurately obtained, but estimates are consistent with the pressure obtained from force balance. The central electron temperature suggested by spectroscopic measurements[2] was T_e~70 *e*V, and the central ion temperature measured from charge exchange energy spectra[3] was T_i=50 *e*V (+40 *e*V,–20 *e*V). The 70-GHz microwave interferometer tracked the chord-averaged electron density to $\langle n_e\rangle \sim 5\times10^{12}$ cm^{-3} at ~0.2 msec before the signal became too small or too noisy. The density was rising when the circuit failed, so values $\langle n_e\rangle \sim 10^{13}$ cm^{-3} are not unreasonable and are consistent with low-q

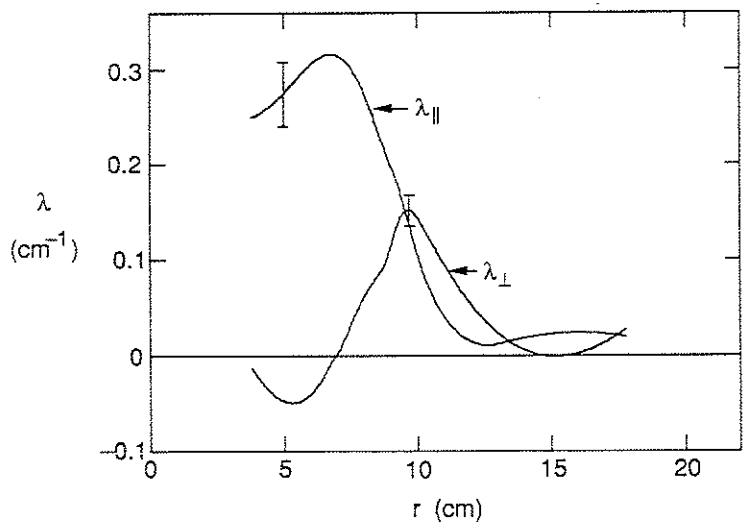

Fig. 4-8. Midplane radial profiles of parallel and perpendicular $\lambda = J/B$.

tokamak plasmas in Tokapole II. Since the pressure dropped sharply at the separatrix, the central density was probably two to three times larger than the chord-averaged value, or $p = n(T_e + T_i) \sim 300 \times 10^{13}$ eV/cm^3. Because the plasma links ~1/2 the ring-generated flux in Tokapole II, roughly one half of the poloidal gap volts drives plasma current. At peak current, $I_p R_p$~50 V. Using the pressure profile to estimate the stored kinetic energy in the plasma and $V_{loop} \geq 50$V, the global energy confinement time within the separatrix, $\tau_E \approx 2\pi R_0 \int p(r) r dr / I_p V_{loop}$, was $\tau_E \leq 20$ μsec.

The sharp drop in both the parallel current and the plasma pressure near the magnetic separatrix leads one to think of the separatrix as a limiter. By definition, it is the boundary between two types of field

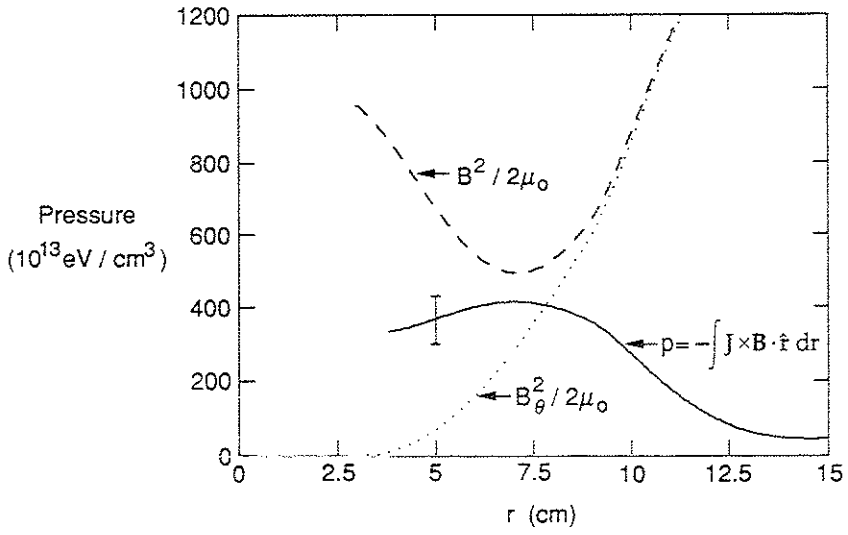

Fig. 4-9. Midplane radial profiles of the plasma pressure (calculated from force balance) and the magnetic pressure.

topology; inside, the flux surfaces are the usual nested, helical structures seen in plasma-current carrying toroidal devices, while outside the field is mostly poloidal as in an internal ring multipole. It is reasonable to think of this magnetic topology as the usual RFP configuration but with a magnetic limiting boundary instead of a material limiting boundary. Unlike the traditional RFP, however, a large, low pressure region fills the space between the edge of the plasma and the stabilizing wall.

The small peak in the poloidal current density (Fig. 4-7) at r≈16 cm is parallel current driven in the common flux region by the applied poloidal electric field. Poloidal Ohmic heating of an octupole plasma using this

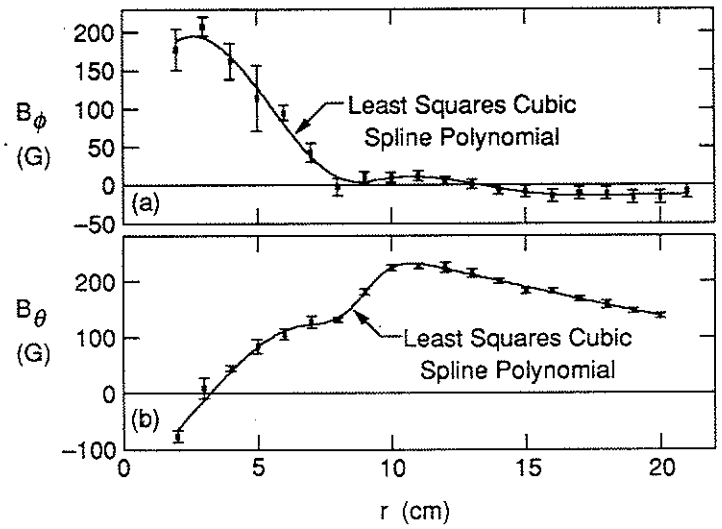

Fig. 4-10. Typical radial profiles of the (a) toroidal and (b) poloidal ($B_\theta - B_{\theta vac}$) components of the midplane magnetic field with poloidal plate limiters in the common flux region (pre-upgrade).

current was studied by Holly, *et al.*, in Tokapole II.[4] In the poloidal divertor RFP experiment, it is an artifact of the toroidal field programming and is probably undesirable since it impedes the penetration of the reversed field; in essence, this current "backwinds" the toroidal field windings.

To reduce this current, stainless steel limiter plates were inserted in the common flux region. Although these plates were designed to eliminate toroidal current and had no toroidal extent, field line helicity would allow some poloidal current reduction. The equilibrium magnetic field profiles obtained in plasmas with the limiters inserted are shown in Fig. 4-10 and

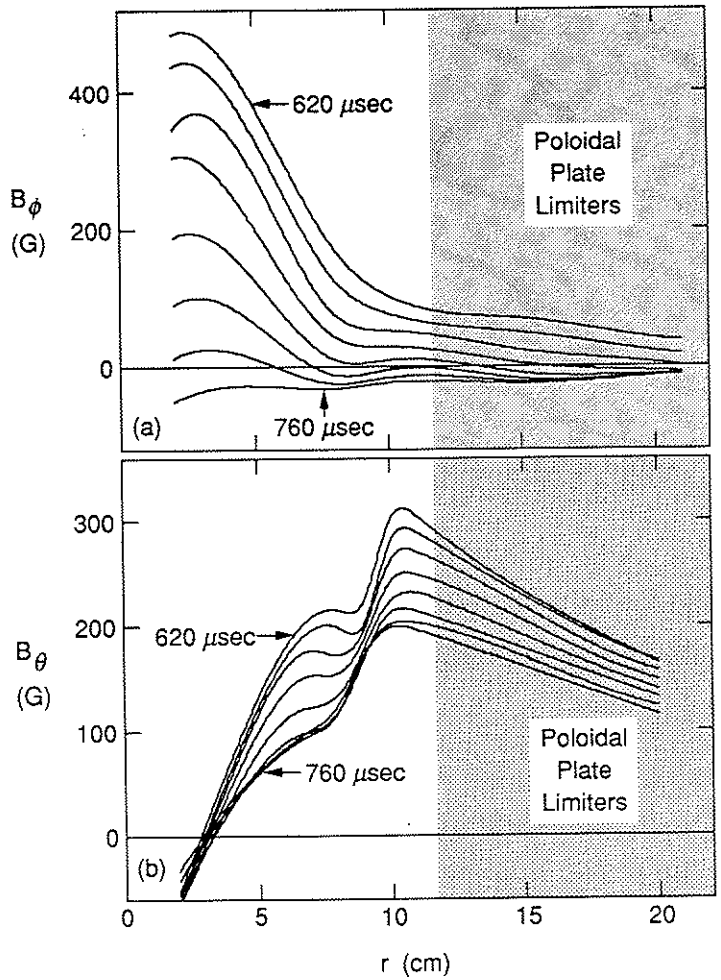

Fig. 4-11. Cubic spline polynomial representations of the radial profiles of the midplane magnetic field with poloidal plate limiters in the common flux region: (a) toroidal and (b) poloidal ($B_\theta - B_{\theta vac}$). The polynomials are plotted at 20 μsec intervals.

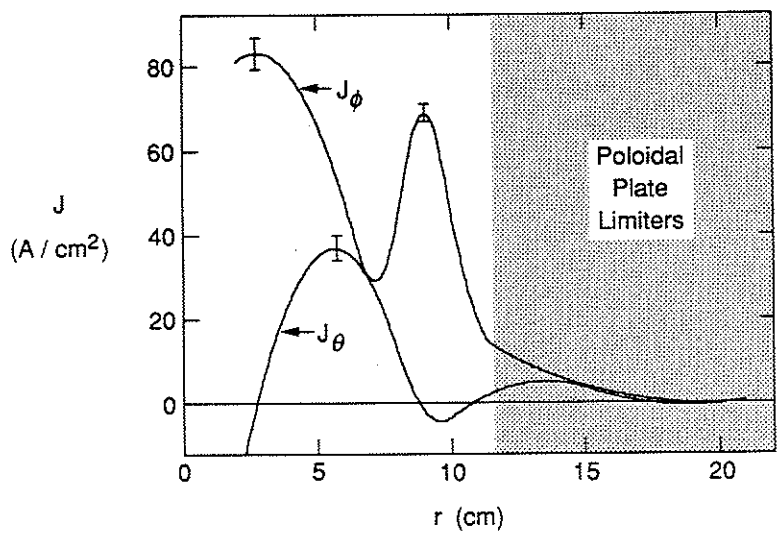

Fig. 4-12. Radial profiles of the midplane current density with poloidal plate limiters in the common flux region derived from the data in Fig. 4-10.

Fig. 4-11. Typical current density and λ profiles for these data are shown in Fig. 4-12 and Fig. 4-13. The common flux parallel current was reduced, and flatter toroidal field profiles were obtained outside the separatrix, but the reversed field equilibria were still transient. The diamagnetic current was more pronounced with the limiters inserted, but the overall character of the equilibrium was similar to the purely magnetically limited case.

Sustainment of RFP equilibria requires the sustainment of the toroidal plasma current. The Tokapole II plasma's large resistance may be due partly to predicted m=1 instabilities, and large electric fields could be

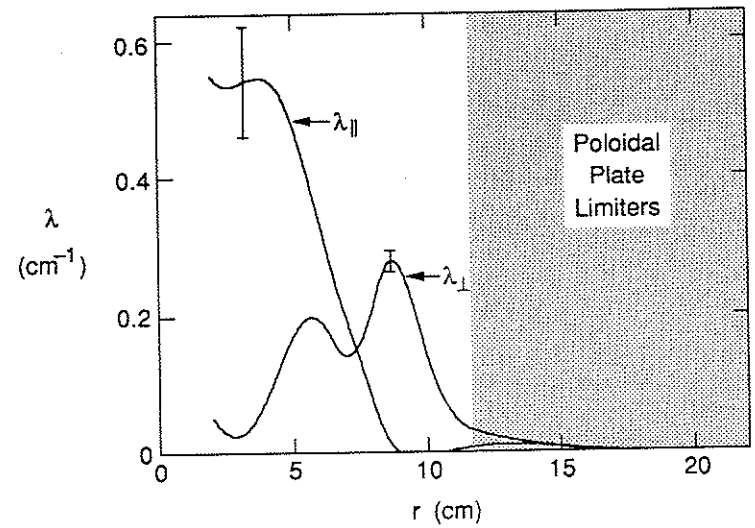

Fig. 4-13. Midplane radial profiles of parallel and perpendicular $\lambda=J/B$ with poloidal plate limiters in the common flux region.

required for sustainment (see Chapter 2). In the experiment, magnetic fluctuations were observed to coincide with the loss of toroidal flux. This is illustrated in Fig. 4-14 where the near-axis toroidal field and its time derivative are plotted. The rate of toroidal field loss increased during bursts of fluctuations. The bursts occurring before the field reversed at the wall were often separated by short periods of relative quiescence, and the dominant frequency of the fluctuation increased in the successive bursts. If the fluctuation represented the rotation of a normal mode of the plasma, and if the rotational velocity was slowly varying in time, then the increasing frequency corresponds to increasing mode number.

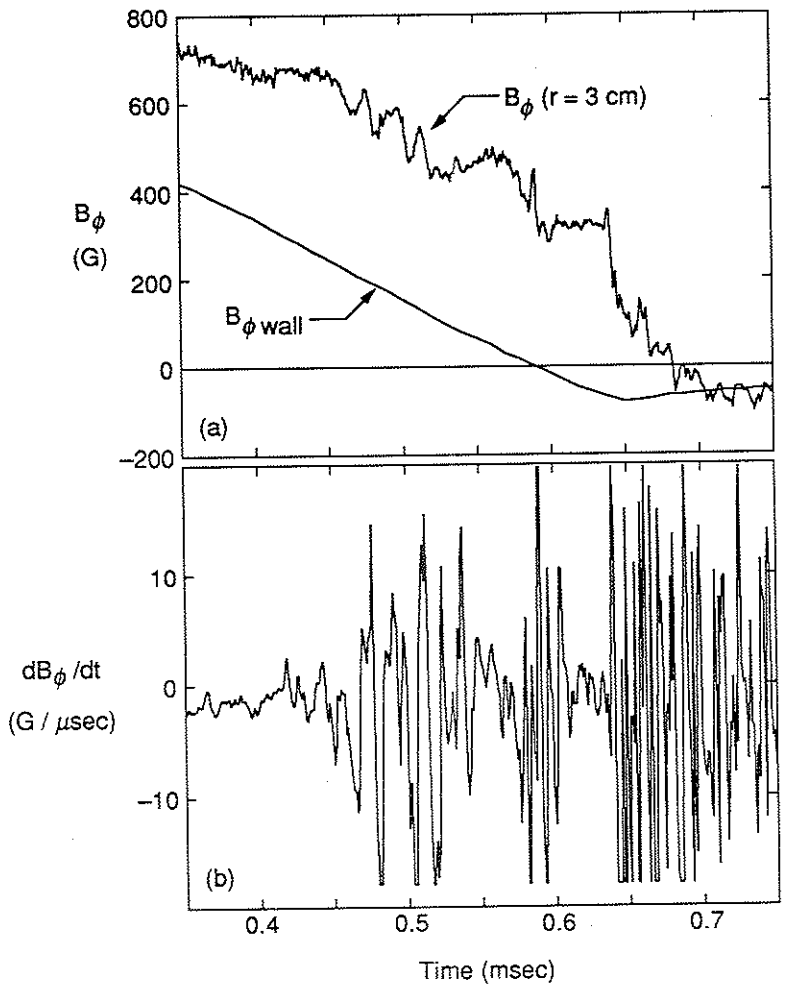

Fig. 4-14. Time evolution of the (a) near-axis toroidal field and (b) its time derivative for a typical plasma (post-upgrade). The frequency bandwidth of the derivative was ~100 kHz.

Unfortunately the character of the fluctuations within the separatrix was different than outside the separatrix, and the identification of mode numbers would require many probes inside the separatrix. The perturbation to the plasma would be large.

The hardware limitations of Tokapole II, *e.g.*, limited poloidal gap voltage, limited maximum ring current, and limited core flux swing, prevented the application of the large toroidal electric field required for plasma current sustainment. To overcome the small-size limitations of Tokapole II, the four-node poloidal divertor RFP experiment was attempted in the Levitated Octupole and eventually in the small ring Octupole device. Before the results from these devices are presented, the results of the operation of Tokapole II with enhanced field errors are presented.

4.1.2 Operation with Enhanced Field Errors

A large, stationary, asymmetric component of the magnetic field was observed in the small ring Octupole poloidal divertor RFP plasma. This asymmetry was detected by magnetic probes placed near the wall on the midplane all at the same minor radius but separated toroidally (see Fig. 4-23, pg. 79). If the plasma was axisymmetric, then the field measured at all locations would have been identical.

An analogous experiment was performed on Tokapole II by placing five probes on the midplane at the toroidal azimuths ϕ=60°, 210°, 240°,

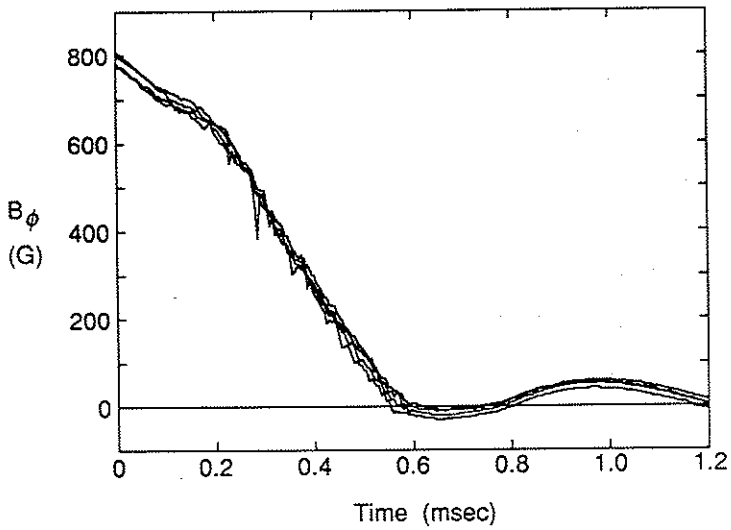

Fig. 4-15. The time evolution of the midplane toroidal field, 12 cm from the wall at five toroidal azimuths; the field is axisymmetric (post-ugrade).

300°, and 330°. The measurements of the toroidal component of the magnetic field, 12 cm from the wall (near the separatrix) are plotted in Fig. 4-15. No large asymmetry was observed.

The asymmetry in the Octupole plasma depended on the details of the field errors at the poloidal gap, and it is possible the asymmetry resulted from a field error. (This is not the most likely explanation since the asymmetry set in abruptly, and it was not observed in divertorless RFP plasmas or in ultra-low-q plasmas). Thinking the field errors in Tokapole II might be too small to initiate such an asymmetry, the poloidal field primary winding was modified to introduce a large m=1 field error at the

poloidal gap. The primary consists of four 20-turn windings, one on each "leg" of the square-cross-sectional core. To get a 40:1 turns ratio in normal operation, the windings are paired in series, and the two pairs are connected in parallel. By removing one or the other pair, large image currents are forced to flow along the poloidal gap, thereby introducing the error field.

With the upper and lower leg primary windings removed from the circuit, measurements of the toroidal component of the magnetic field were obtained. The results in vacuum and in plasma, 10 cm from the wall on the midplane at toroidal azimuths $\phi = 60°$, 240°, 300°, and 330°, are shown in Fig. 4-16. The field error was apparent in the spread of the vacuum measurements, but with plasma, no additional asymmetry was observed. Since the field error degraded the plasma current, a smaller field error was tested by inserting a small inductor in series with one of the primary winding pairs. This error was less perturbing to the current, but again, no additional asymmetry was observed.

If a large, stationary asymmetry could have been produced in the Tokapole II RFP plasma by this type of experiment, then it would be plausible to conclude the asymmetry in the Octupole plasma was field-error-driven. Little can be concluded from the null result, since other field errors in the Octupole, *e.g.*, those associated with the toroidal field system, could not be recreated on Tokapole II.

Although not stationary, substantial magnetic perturbations ($\delta B/B \leq 20\%$) were observed near the center of the Tokapole II plasmas

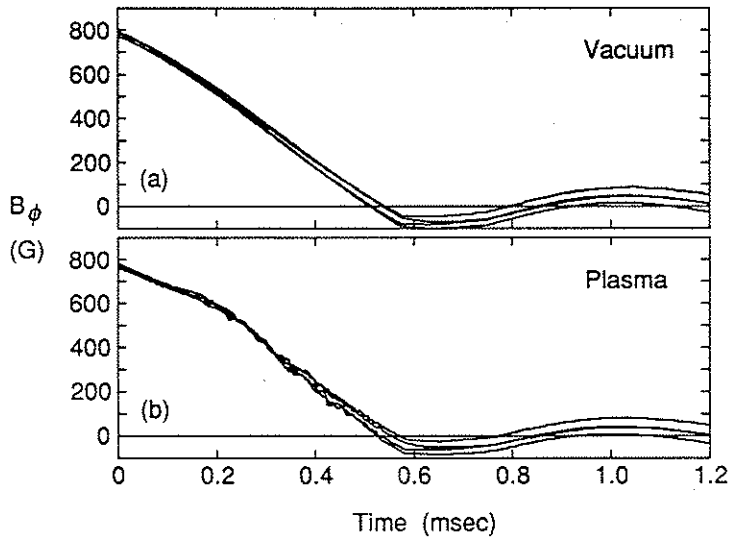

Fig. 4-16. Time evolution of the midplane toroidal field, 10 cm from the wall at four toroidal azimuths after field error enhancement: (a) in vacuum and (b) with plasma (post-upgrade).

(Fig. 4-14). If the stationary asymmetry in the Octupole plasma was generated by plasma instability, then the magnetic perturbations observed in both the Tokapole II and Octupole plasmas may represent similar instability. The stationary nature of the perturbation in the Octupole plasma possibly resulted from a specific interaction with the field errors in that device that had no counterpart in Tokapole II. This possibility is discussed in more detail in Chapter 5.

4.2 LEVITATED OCTUPOLE DIVERTOR RFP RESULTS

A typical four-node poloidal divertor RFP discharge on the Levitated Octupole is shown in Fig. 4-17. Like the Tokapole II plasmas, only transiently reversed equilibria were obtained. Fig. 4-18 shows measurements of the toroidal component of the magnetic field at the wall and at 5 cm from

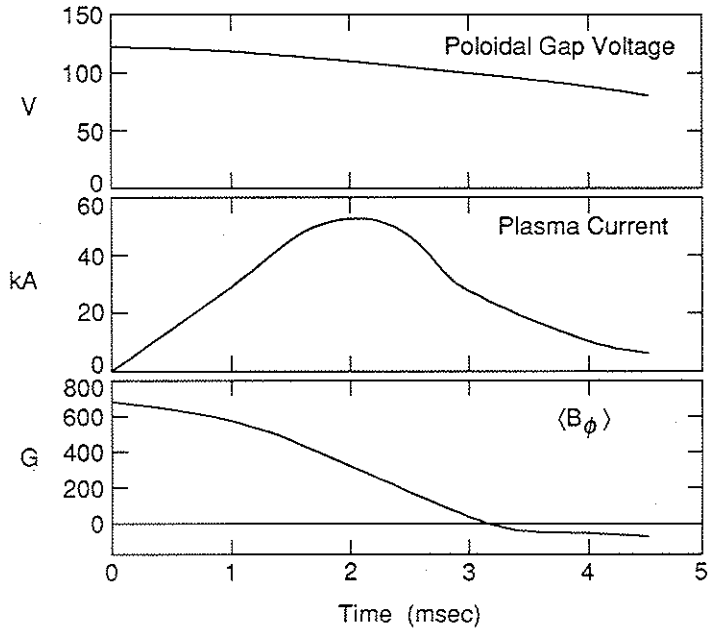

Fig. 4-17. Time evolution of basic electrical quantities for a typical poloidal divertor RFP discharge in the Leviated Octupole.

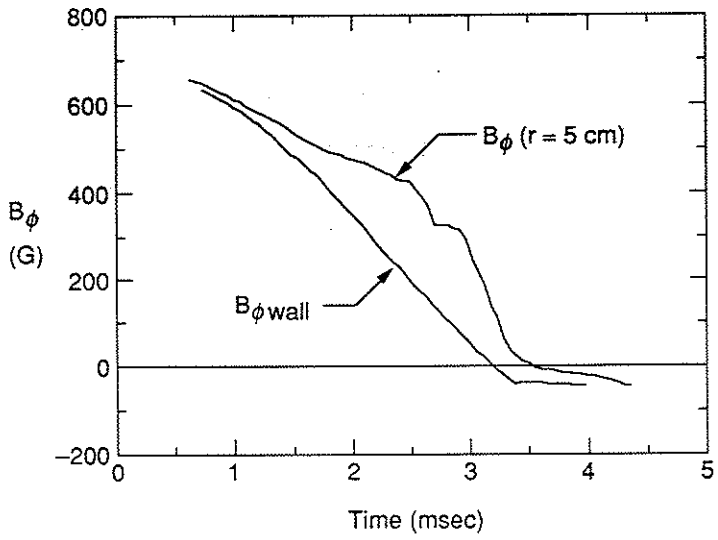

Fig. 4-18. Time evolution of the toroidal field near-axis and the toroidal field at the wall in a typical poloidal divertor RFP plasma in the Levitated Octupole.

the geometric axis on the midplane; the behavior was similar to that of Tokapole II (Fig. 4-4), except the transient reversal period was ~200 μsec.

After only ~2 months of operation, this experiment ended abruptly when severe arcing at the poloidal gap caused the failure of the vacuum seal. The rings were removed to facilitate the development of a suitable gap protection scheme in the noncircular RFP operation of the divertorless device.[5]

4.3 SMALL RING OCTUPOLE DIVERTOR RFP RESULTS

4.3.1 Equilibrium Properties

The noncirular RFP studies ended when new, smaller rings were installed in the Octupole vacuum vessel. The rings in the Levitated Octupole were physically very large. As a result, the plasma linked 80% of the ring-generated flux, substantially reducing the electric field which maintained the plasma current. The new rings were smaller, and the plasma linked only 13% of the ring-generated flux. In this sense, they were optimized by minimizing their mutual inductive coupling to the plasma; the constraint was sufficient material strength to withstand the magnetic forces.

The time evolution of the basic electrical quantities, central-chord line-averaged density, and central electron temperature for a typical 135-kA small ring Octupole four-node poloidal divertor discharge is shown in Fig. 4-19. The density was measured by a 140-GHz microwave interferometer, and the central temperature was measured by a single-point Thomson scattering system.[6] The toroidal field remained reversed at the wall for ~1.2 msec while the average toroidal field, measured by a flux loop located just inside the wall, remained nonreversed.

Radial profiles of the magnetic field were obtained on the midplane at toroidal azimuths of ϕ=45°, 135°, and 225° relative to the poloidal gap using three magnetic probes. The perturbational effect of the probes is

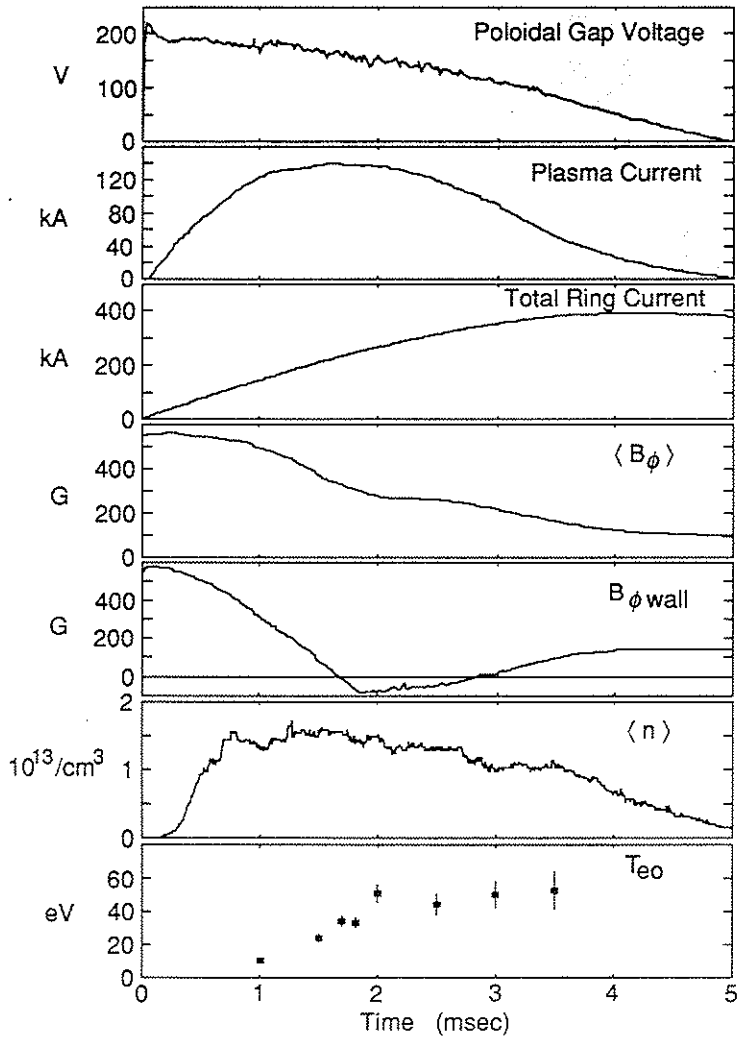

Fig. 4-19. Time evolution of electrical quantities, central-chord line-averaged density, and central electron temperature for a typical small ring Octupole poloidal divertor RFP plasma.

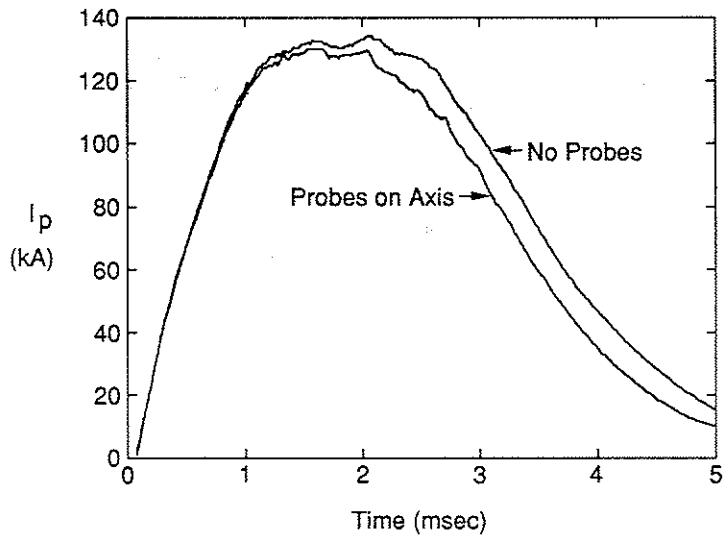

Fig. 4-20. Comparison of the plasma current with and without magnetic probes on-axis in the small ring Octupole.

illustrated in Fig. 4-20, which shows a comparison of the plasma current waveforms for an unperturbed plasma and a plasma with the three probes inserted to the axis. As for the Tokapole II plasmas, the discharge was shortened slightly with the probes inserted. To form a measurement of the equilibrium magnetic field, the probes were located at the same midplane radius, and the components measured at the three azimuths were averaged. Also, the data from several shots were averaged to reduce shot-to-shot irregularities. The results at 1.6 msec (~150 μsec before toroidal field reversal at the wall) are shown in Fig. 4-21. The theoretical location of the magnetic separatrix, estimated from numerical equilibrium calculations, is

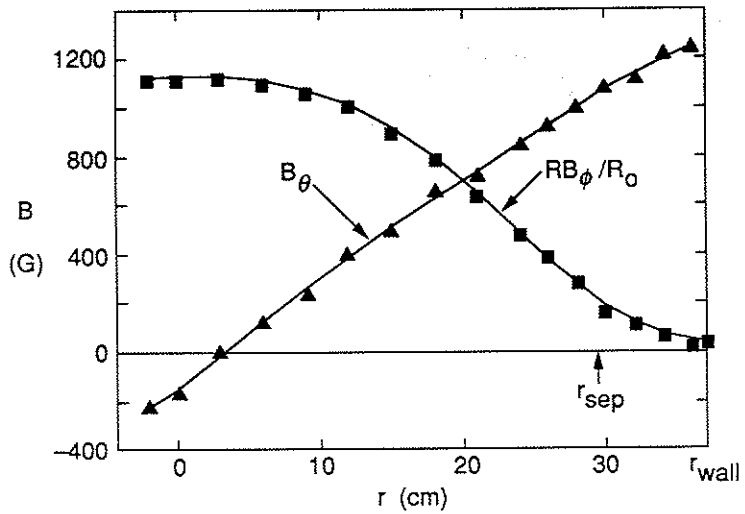

Fig. 4-21. Radial profiles of the toroidal and poloidal components of the midplane magnetic field. The theoretical radius of the separatrix is r_{sep}=29.5±1.0 cm. The wall radius is r_{wall}=37 cm.

indicated. The time evolution of the radial profiles is shown in Fig. 4-22. For times up to ~1.75 msec, the radial (horizontal) component was small ($B_r \leq 20$ G), indicating a vertically centered plasma, and the magnetic axis was shifted outward ~3 cm from the geometric axis. The rise of the poloidal field out to the wall resulted from the flux compression created by the wall indentations on the midplane. This noncircularity prevents the use of Eq. 4-4 at large radii to determine the toroidal current density profile. Likewise the equilibrium λ and pressure profiles cannot be obtained as they were for the Tokapole II plasmas.

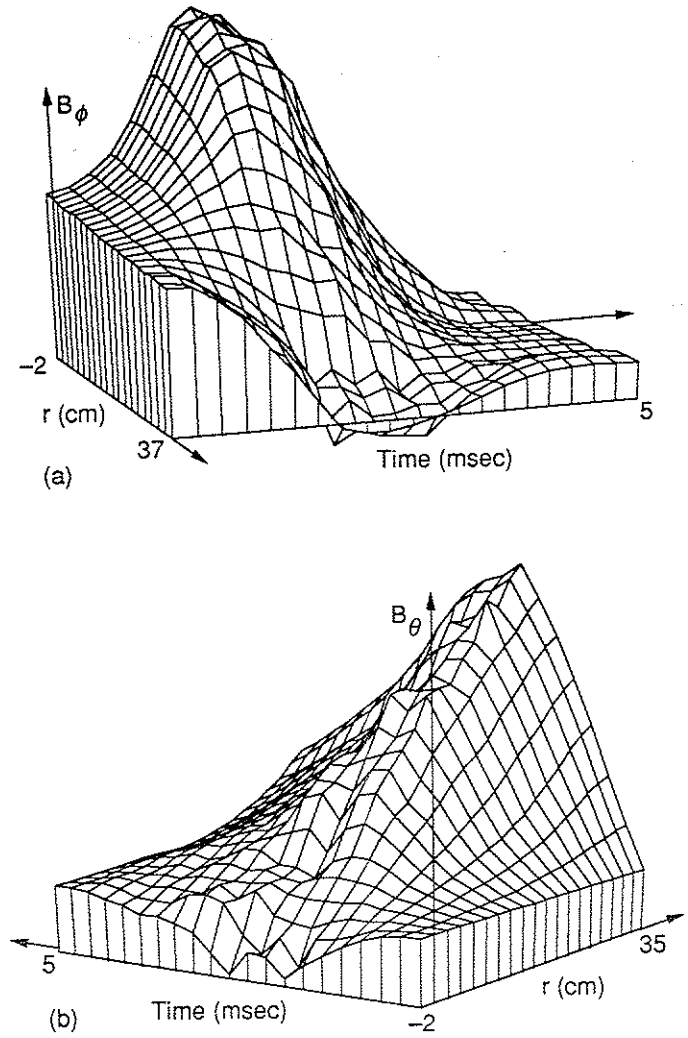

Fig. 4-22. Time evolution of the (a) toroidal and (b) poloidal components of the midplane magnetic field radial profiles.

The on-axis, toroidal one-turn loop voltage at peak plasma current was estimated using the circuit model described in Section 3.3.1:

$$V_{loop} = 2\pi R_o E_{\phi o} \approx V_{pg} - \alpha d\Phi_r/dt = 136 \text{ V}. \qquad 4\text{-}5$$

The term $\alpha d\Phi_r/dt$ represents the inductive voltage due to the portion, α, of the total ring-generated poloidal flux, Φ_r, which links the plasma, and was estimated to be ~13 V from numerical equilibrium calculations and the measured ring current. If a simple Ohm's law applies, then on axis $E_{\phi o} = \eta_o J_{\phi o}$. Although Eq. 4-4 for $J_\phi(r)$ is not valid at large radii, near the axis cylindrical symmetry is a reasonable approximation, and $J_{\phi o}$ may be calculated. From the measurements of V_{loop} and $J_{\phi o}$, η_o was evaluated, and when compared with the Spitzer resistivity[7] given by the measured electron temperature for Z=1, it was found that $\eta_o/\eta_{Spitzer}$ ~12. No measurement of the effective charge state, Z_{eff}, was made, but the value required to produce a classical resistivity is large for a plasma with an electron temperature T_e~50 eV. It may be that nonclassical effects, *e.g.*, fluctuations or field errors, enhanced the loop voltage. Taking n~10^{13} cm^{-3}, T_e~T_i~50 eV, V_{loop}=136 V, and I_p=135 kA, an estimate of the global energy confinement time within the separatrix (cross-sectional area A_{sep}≈ 0.38 m^2) at peak plasma current is

$$\tau_E \approx 2\pi R_o A_{sep} n(T_e + T_i)/I_p V_{loop} = 30 \ \mu\text{sec}. \qquad 4\text{-}6$$

This small confinement time may also be the result of fluctuations or field errors.

4.3.2 Asymmetries

Despite the well-behaved appearance of the quantities shown in Fig. 4-19, the local measurements of the magnetic field uncovered a large asymmetric component which set in about the time when the spatially averaged toroidal field reversed at the wall. Seven magnetic probes were distributed toroidally around the device and were located a few centimeters from the wall on the midplane to check axisymmetry. The measurements of the toroidal and poloidal components of the magnetic field are plotted in Fig. 4-23 for a typical plasma. This asymmetry was always observed and was stationary (varying on the equilibrium time scale). The magnitude of the magnetic perturbation was $\delta B/B$~40%.

The poloidal mode structure of the asymmetry was dominated by the poloidal mode number m=1. To illustrate this, midplane radial profiles of the radial magnetic field, B_r, measured at ϕ=135° and ϕ=225° are plotted in Fig. 4-24. The data points are B_r, time-averaged from 2.5–3.0 msec, measured in plasmas in which the asymmetry was nearly identical as determined by matching signals from stationary probes placed near the wall. These particular data should represent the profiles that would be measured in a single, typical plasma. Because B_r peaks on axis, there must have been a large m=1 component. The transverse magnetic signals from a

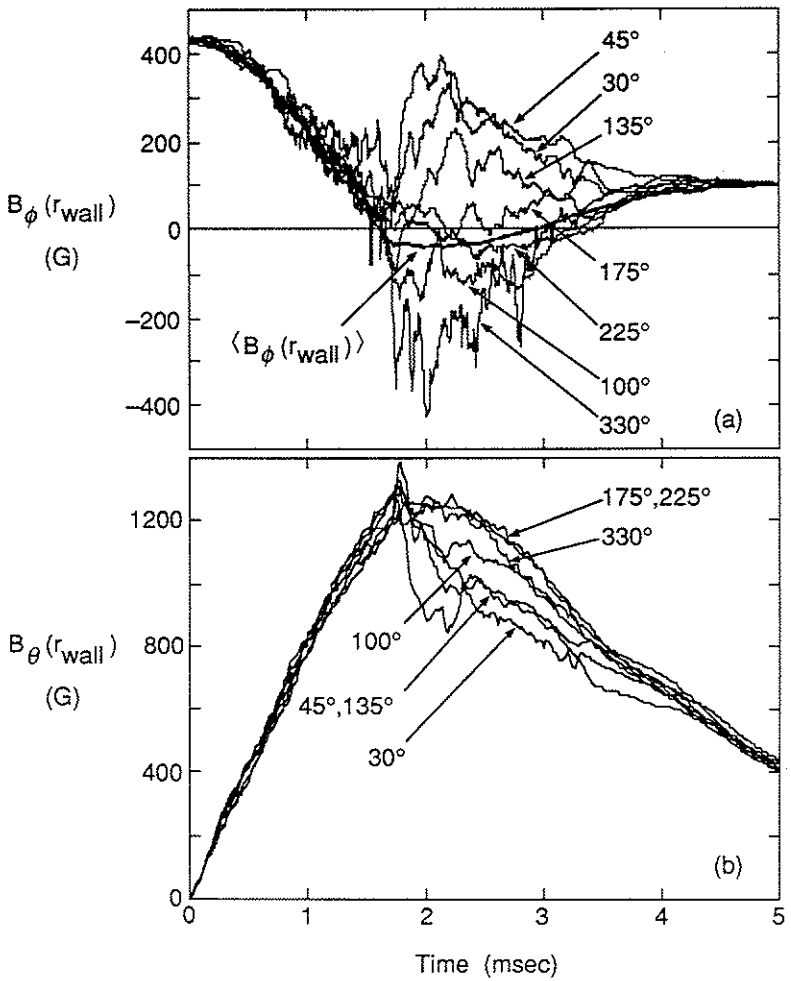

Fig. 4-23. Time evolution of the (a) toroidal and (b) poloidal components of the midplane magnetic field measured 2.0 cm from the wall at seven toroidal azimuths. $\langle B_\phi(r_{wall}) \rangle$ is the spatially averaged toroidal field at the wall calculated from the total wall current.

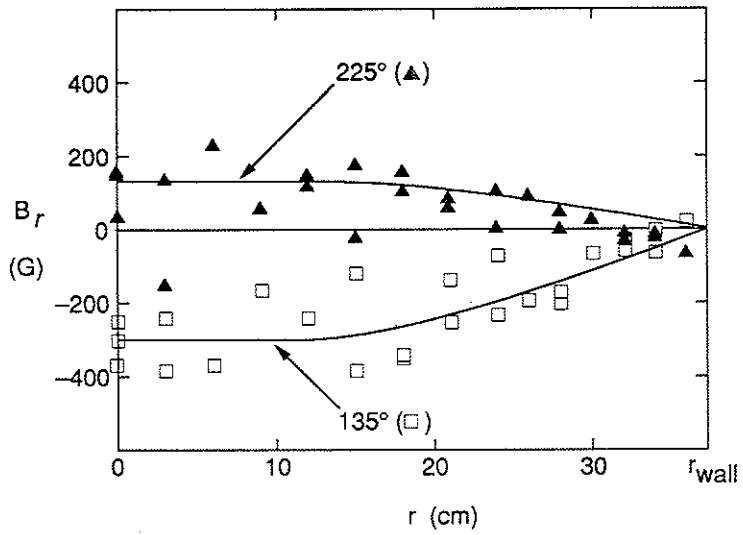

Fig. 4-24. Measurements of the radial (horizontal) component of the midplane magnetic field at ϕ=135° and ϕ=225°.

set of six probes located near the wall at ϕ=225° but separated poloidally exhibited a dominant m=1 dependence, although m=2 and m=3 were only ~50% smaller. Since the noncircular vacuum vessel wall distorts the perturbation generated by internal m=1 plasma motion, larger mode numbers—especially m=2 and m=4—are expected to be detected near the wall; it is likely that m>1 modes were small internally.

The toroidal mode structure was more complicated. Presuming a single mode, phase measurements using the signals from closely spaced probes on the midplane, like those at ϕ=30°, 45°, and 330° shown in Fig. 4-23, suggest a toroidal mode number of $|n| \approx 4$–6, but the signals at all locations do not, in general, fit a single mode. Unfortunately, there were

too few measurements to perform a proper Fourier analysis if mode numbers $|n| \geq 4$ were present. From the equilibrium field profiles measured just before the onset of the asymmetry, the axis safety factor was $q_o = 0.19 \pm 0.01$, so modes with $m=1$, $-n \geq 6$ would have been internally resonant.

Although little is known about the magnitude of the toroidal mode numbers, the sense of the pitch of the modes can be inferred from the relationship

$$\tilde{B}_\theta\left(r=r_{wall},\theta=midplane,\phi\right) = \frac{m}{n}\frac{R_{wall}}{r_{wall}}\tilde{B}_\phi\left(r=r_{wall},\theta=midplane,\phi\right) \qquad 4\text{-}7$$

resulting from the boundary condition that the normal component of the perturbed current density vanish at the conducting wall. Eq. 4-7 was derived specifically for locations on the midplane for the case of a single mode using Ampere's law to relate the perturbed current density to the perturbed magnetic field, $\tilde{B}$. It implies that measurements of $\tilde{B}_{\theta wall}$ and $\tilde{B}_{\phi wall}$ at any toroidal azimuth would lie on a line with slope proportional to m/n when plotted as $\tilde{B}_{\theta wall}$ versus $\tilde{B}_{\phi wall}$. If the slope is negative ($n<0$), then the mode pitch is the same sense as the equilibrium field near the axis.

If more than one mode exist, Eq. 4-7 applies to each mode seperately, but the linear relationship between the *total* field components $\tilde{B}_{\theta wall}$ and $\tilde{B}_{\phi wall}$ is destroyed. If the modes are closely spaced in m and n, though, the points $\tilde{B}_{\theta wall}$ versus $\tilde{B}_{\phi wall}$ at all toroidal azimuths differ only slightly

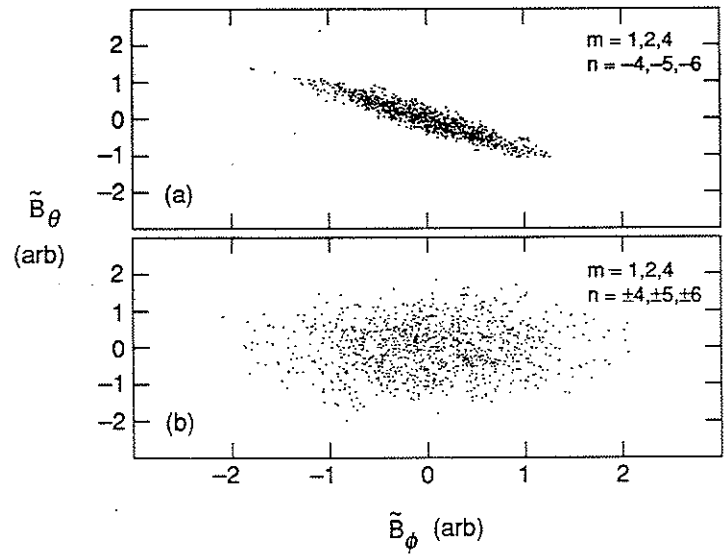

Fig. 4-25. $\tilde{B}_{\theta wall}$ versus $\tilde{B}_{\phi wall}$ for two hypothetical cases of asymmetry: (a) similarly pitched modes and (b) oppositely pitched modes.

from the single-mode linear relationship, and the sense of pitch for these similar modes can still be inferred. This is illustrated in Fig. 4-25 which shows $\tilde{B}_{\theta wall}$ versus $\tilde{B}_{\phi wall}$ for two *hypothetical* cases of asymmetry. In Fig. 4-25a, nine modes were superimposed using the combinations of m=1, 2, & 4 and n= –4, –5, & –6. The m=1 modes have equal amplitude in the sense that $(\tilde{b}_{\theta mn}^2 + \tilde{b}_{\phi mn}^2)$ is constant, where $\tilde{b}_{mn}$ is the amplitude of the m,n mode, and $\tilde{B}_{jwall} = \sum_{mn}\tilde{b}_{jmn}\cos(m\theta + n\phi + \delta_{mn})$. The m=2 and m=4 modes have respectively 50% and 25% of the m=1 amplitude. The modes were mixed with random phases, δ_{mn}, and each plotted point represents $\tilde{B}_{\theta wall}$ versus $\tilde{B}_{\phi wall}$ at randomly selected toroidal azimuths. The points do not

form a line, but a linear trend is preserved. In Fig. 4-25b, nine additional modes were included using the combinations of m=1, 2, & 4 and n= 4, 5, & 6. These modes have pitch opposite the original nine and cause a large spreading or randomization of the $\tilde{B}_{\theta wall}$ versus $\tilde{B}_{\phi wall}$ points.

In the experiment, all the measurements of $\tilde{B}_{\theta wall}$ versus $\tilde{B}_{\phi wall}$ were nearly linearly related. This is illustrated in Fig. 4-26 where $B_{\theta wall}$ and $B_{\phi wall}$, time averaged over a 300-μsec interval during the period of the asymmetry, are plotted for two plasmas with different locked phases of the asymmetry. (Plotting the total fields $B_{\theta wall}$ and $B_{\phi wall}$ simply adds an offset equal to the symmetric portion of the field). Any line that reasonably fits these data has a negative slope, indicating the dominant mode—or band of modes—was internally resonant or internally nonresonant. In addition, when the locked phase changed, the points $B_{\theta wall}$ versus $B_{\phi wall}$ moved along the same line.

The stationary nature of the asymmetry suggested that field errors might be important; large field errors existed at both the poloidal and toroidal gaps. The poloidal gap was instrumented with eight large coils, each covering one-eighth of the poloidal circumference, sensitive to the error (perpendicular) flux passing through the gap. The spatial Fourier amplitudes of the m=0–4 components of the measured error flux, normalized to the total poloidal flux, for a typical plasma are shown in Fig. 4-27. Many attempts were made to correct this error by adjusting the poloidal field primary current distribution, but no substantial improvement was obtained, and the asymmetry persisted. The elimination

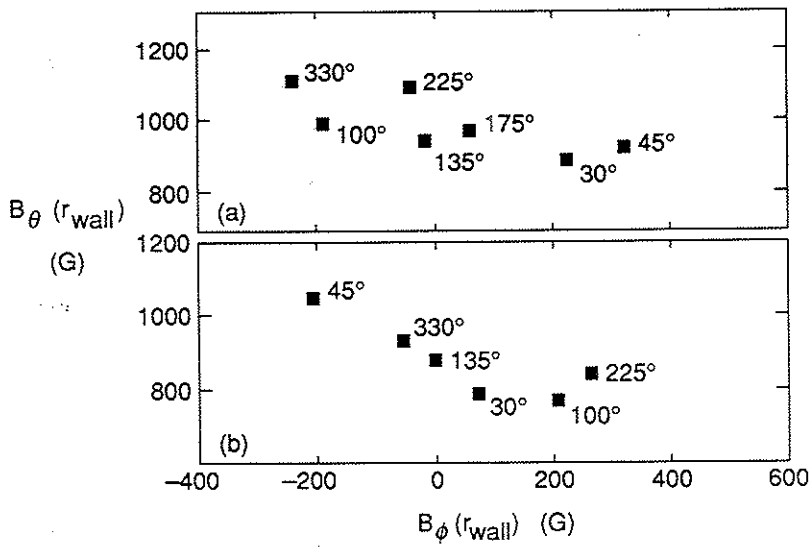

Fig. 4-26. The poloidal versus the toroidal component of the midplane magnetic field near the wall, time-averaged from 2.4–2.7 msec for (a) the most often occuring locked phase of the asymmetry and (b) a different locked phase.

of the poloidal gap error was an inherently difficult task since the device was designed for the current distribution of a pure octupole field.

Although the adjustments of the primary current distribution failed to eliminate the asymmetry, they did alter the detailed structure of it. Magnetic probe signals which were typically "positive" for one configuration of the primary became typically "negative" for a different configuration, *i.e.*, the asymmetry was phase-locked to the poloidal gap field error. One may speculate that the shape of the conducting wall may

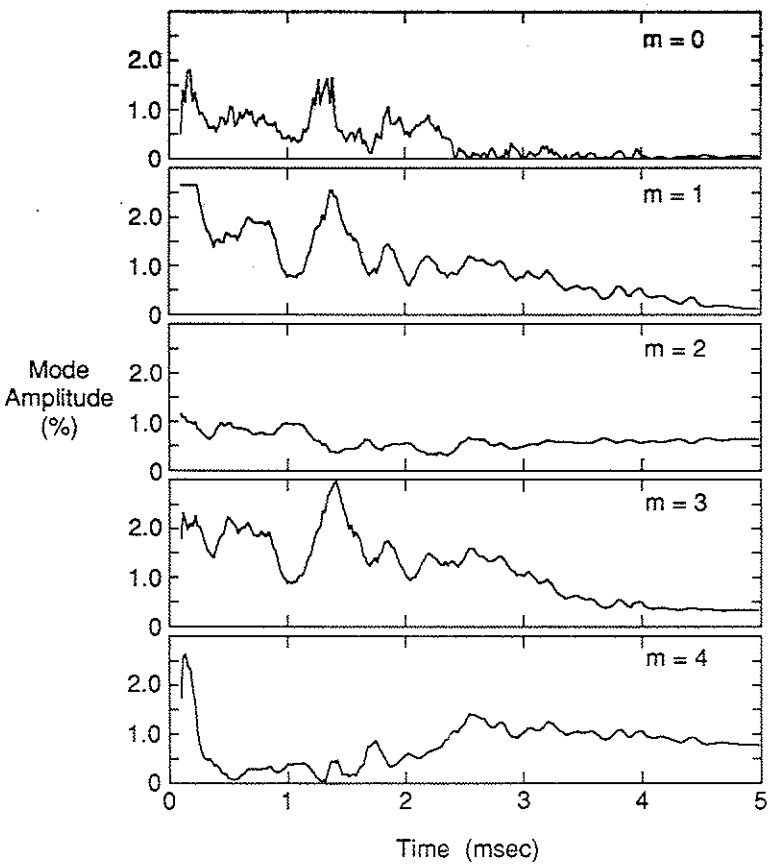

Fig. 4-27. Amplitudes of the m=0–4 Fourier components of the normalized error flux at the poloidal gap in the small ring Octupole vacuum vessel. The fluxes are normalized to the total poloidal flux.

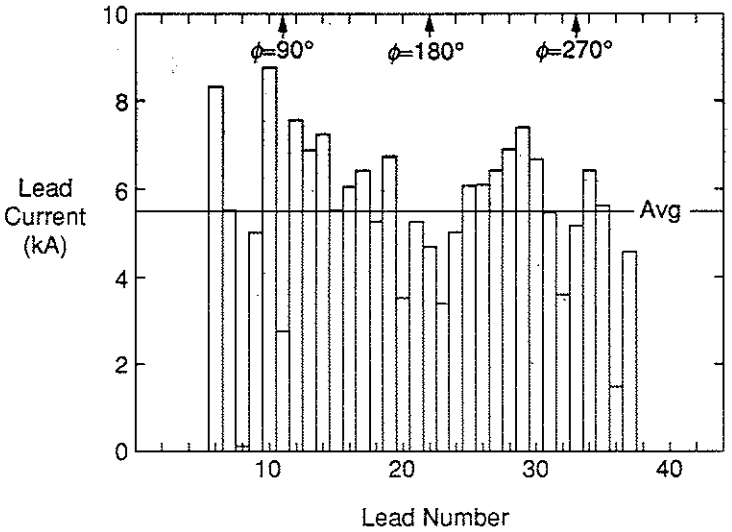

Fig. 4-28. Measurements of the current at 1.0 msec in 32 of the 44 leads in the toroidal field system. The average value is proportional to the average toroidal field at the wall.

have prompted this behavior since the protruding "noses" were much closer to the plasma than other locations around the gap, preferentially exposing the plasma to the local error structure.

Large field errors at the toroidal gap resulted from nonuniform current in the toroidal field leads. Measurements of the current in 32 of the 44 leads at 1.0 msec are shown in Fig. 4-28. The Fourier composition of the current is shown in Fig. 4-29. Although the lead current was irregular, the vacuum toroidal field was relatively axisymmetric at all locations where it was measured; apparently the *wall* current was uniform away from the

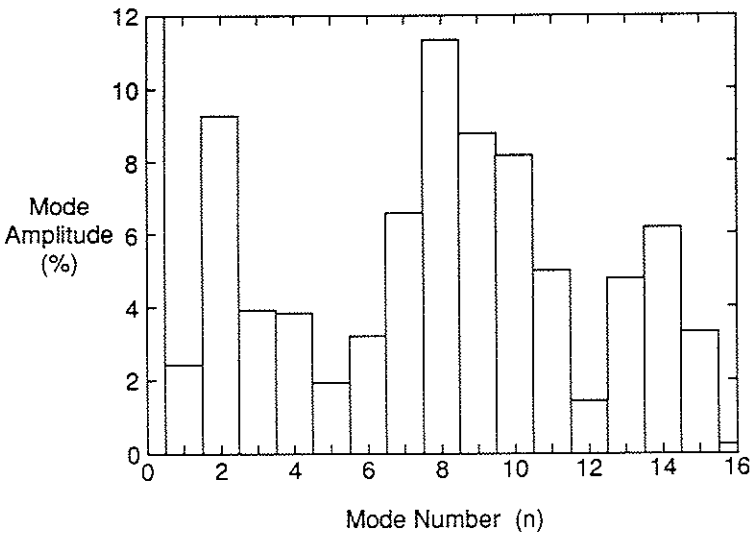

Fig. 4-29. Amplitudes of the n=0–16 Fourier components of the normalized lead current shown in Fig. 4-28. The current is normalized to the n=0 component or average lead current.

gap. The irregular distribution of the lead current probably resulted from the mutual inductive coupling of the many leads. The system was designed to operate at a lower frequency, *i.e.*, in the resistive limit, providing a steady-state field for experiments in the Leviated Octupole. The fast programming of the toroidal field for RFP formation was never intended, and significant improvement would have required a new system.

Several observations suggest that the plasma asymmetry was probably not initiated by field errors, but was more likely the result of an instability. First, most of the nonreversed portion of the discharge was relatively symmetric, and the abrupt onset of asymmetry indicates rapid motion of the plasma. Also, ultra-low-q plasmas (q_{edge}~0.3) produced in this same device were relatively symmetric the entire duration of the discharge (~5 msec). Finally, divertorless RFP plasmas produced in the same vacuum vessel with similar field errors did not exhibit stationary asymmetries, although large amplitude, high-frequency fluctuations were observed.[5] (The divertorless plasma measurements were made at only one or two locations, and by chance, a stationary perturbation with a node at these locations would not have been detected.) Still, it is difficult to state definitively that elimination of the field errors would not have prevented the perturbation.

The asymmetry might be the result of an unstable, nonreversed equilibrium. It was observed to set in about the time when the spatially averaged toroidal field reversed at the wall, but at this time, the toroidal field was a little more positive at the separatrix (implying the separatrix was not a perfect current limiter). It is best described by mode numbers m=1 and n ~ –5. Although the poloidal divertor configuration is highly noncircular, the linear and nonlinear MHD stability of a cylindrical plasma far from a stabilizing wall (Chapter 2) should serve as a guide to predict the types of current-driven instability expected for analogous equilibrium conditions in the small ring Octupole plasmas. Indeed, the linearly unstable m=1 modes in the region $\lambda_0 a \leq 2.4$ (nonreversed equilibria) and

$k/\lambda_o < 0$ (internally resonant or nonresonant modes) in Fig. 2-5b match the asymmetry mode structure and equilibrium conditions at the time asymmetry struck the small ring Octupole plasma. In cylindrical plasmas, MHD predicts the most unstable modes to be those slightly nonresonant and resonant near the axis. If this holds true in the poloidal divertor configuration, then the most unstable mode at the time the asymmetry began would have been m=1, n= –5, recalling that the axis safety factor was $q_0 = 0.19$ just before the asymmetry set in.

Circular RFP plasmas bounded by a relatively thin vacuum layer exhibit large fluctuation amplitudes during the nonreversed setup phase, but the fluctuations do not prevent the formation of relatively quiescent RFP equilibria. In the poloidal divertor experiment, the large vacuum region probably leads to a relatively large range of unstable equilibria and to increased growth rates and nonlinearly saturated amplitudes of the unstable modes. The failure of the poloidal divertor plasma to obtain a quiescent, RFP-like equilibrium may be due to excessively large perturbations generated late in the setup phase. Without an equivalent stability analysis or simulation which includes the poloidal divertor configuration, the details of the MHD stability of the poloidal divertor configuration remain uncertain.

REFERENCES

1 R. J. Groebner, Ph.D. Thesis, University of Wisconsin-Madison (1979).

2 R. N. Dexter, private communication.

3 T. A. P. Casavant, University of Wisconsin-Madison PLP 966 (1985).

4 D. J. Holly, S. C. Prager, and J. C. Sprott, Phys. Fluids **26**, 3435 (1983).

5 A. Almagri, S. Assadi, R. N. Dexter, S. C. Prager, J. S. Sarff, and J. C. Sprott, Nucl. Fusion **27**, 1795 (1987).

6 D. J. Den Hartog and R. N. Dexter, University of Wisconsin-Madison PLP 1023 (1987).

7 L. Spitzer, Jr. and R. Harm, Phys. Rev. **89**, 977 (1953).

CHAPTER 5

SUMMARY AND CONCLUSIONS

The experimental results of the attempts to form four-node poloidal divertor reversed field pinch plasmas in Tokapole II, the Levitated Octupole, and the small ring Octupole are:

Tokapole II

1. Transient, RFP-like equilibria were obtained for ~100 μsec.
2. As expected, the separatrix was observed to limit magnetically the plasma current density and the plasma pressure. A large diamagnetic current was observed near the separatrix owing to the sharp drop in the pressure.
3. Bursts of magnetic fluctuations ($\delta B/B \sim 20\%$) coincided with the rapid loss of toroidal flux on-axis. This implies a concomitant rapid loss of (parallel) plasma current.
4. Operation of Tokapole II with enhanced m=1 poloidal gap field errors did not generate asymmetry analogous to that observed in the small ring Octupole plasmas.

Levitated Octupole

1. Only preliminary data were obtained in this configuration, but the results indicated qualitatively similar behavior to the results obtained on Tokapole II. Transient, RFP-like equilibria were obtained for ~200 μsec.

Small Ring Octupole

1. Encouraging, nearly steady-state, RFP-like, globally averaged equilibria were obtained for periods up to 1.5 msec.
2. Local measurements of the magnetic field uncovered a large, stationary, asymmetric component of the field ($\delta B/B \sim 40\%$) which set in late in the setup phase of the discharge. This asymmetry was predominantly composed of internally nonresonant or resonant modes with a poloidal mode number m=1 and toroidal mode numbers $n \sim -5$. It was always observed, independent of operating conditions (except the toroidal field programming).
3. The equilibrium just before the asymmetry set in was well-behaved, and measurement of the axis safety factor indicated modes with m=1 and $-n \geq 6$ would have been resonant.
4. Large field errors existed at the poloidal and toroidal gaps. Manipulation of the poloidal gap error correlated with changes in the stationary phase of the asymmetry. Small reductions in the magnitude of the error flux at the poloidal gap did not eliminate the asymmetry.
5. This stationary asymmetry was *not* observed in ultra-low-q divertor plasmas or in divertorless plasmas produced in the same vacuum vessel with similar field errors at the gaps. Therefore, it is likely the asymmetry resulted from an unstable, nearly reversed, four-node poloidal divertor equilibrium.

The asymmetry in the small ring Octupole poloidal divertor RFP plasma was measured to have properties consistent with MHD-predicted m=1, current-driven instability of a non-reversed cylindrical plasma bounded by a vacuum region and a distant, stabilizing wall. Equivalent calculations in the four-node poloidal divertor geometry have not been performed, so only the general implications of the cylindrical geometry results can be trusted in this highly noncircular divertor configuration.

The stationary nature of the asymmetry and its observed correlation with the details of the poloidal gap error certainly suggest an alternate interpretation that the asymmetry was field-error-generated. To explain the global structure, the most likely description in terms of a pure field error effect is the sudden formation of a magnetic island. To generate the large perturbed radial field on-axis, the responsible field error would have resonated near the axis, and the toroidal mode number would have been $n \geq 6$. The error current in the toroidal field leads was broadly distributed in n, so error fields with the appropriate helicity existed.

The problem with this interpretation is the lack of similar stationary asymmetry in the ultra-low-q divertor plasmas and the divertorless, non-circular RFP plasmas. Also, no single mode greatly dominated the error field structure, and islands with a variety of helicities—in particular those with n<6—would be expected. Still, the magnitude of the error field was uncomfortably large, and it is impossible to definitively eliminate island formation as the explanation of the asymmetry. The stationary nature of the asymmetry can also be explained as phase locking of an instability-generated magnetic perturbation which interacted with the field error.

The lack of similar asymmetry in the Tokapole II plasmas, even in the presence of an enhanced poloidal gap field error, does not support or contradict the interpretation of the Octupole plasma asymmetry as field-error-generated. Not all of the Octupole magnetic field errors could be recreated on Tokapole II. The toroidal field in Tokapole II is produced by current in a wire, and the toroidal mode numbers n=24 and n=4 are expected to dominate the toroidal gap error structure. This is quite different from the broad spectrum of modes that existed in the Octupole.

The bursts of large magnetic fluctuations observed near the center of the Tokapole II plasmas probably represent periods of instability. Presuming this to be the case, the Tokapole II and the small ring Octupole plasmas might have suffered similar instability. (Too few data exist for the Levitated Octupole plasmas to make a similar statement about that configuration.) The fluctuating nature of the Tokapole II magnetic perturbation—actually the more common manifestation of a normal mode since the plasma usually rotates—might indicate the lack of an analogous field error interaction causing the perturbation to lock to the wall. The plasma in the small ring Octupole was closer to the wall, particularly at the "noses," and the normalized field errors were about five times larger in that device.

If the presumed instability of the Tokapole II and small ring Octupole plasmas resulted from the lack of a nearby stabilizing boundary, then this research implies that the proper placement of the wall is crucial to RFP generation and sustainment. For future RFP designs which separate the plasma from the wall, it will be important to know the allowable

vacuum layer thickness which does not deleteriously affect the RFP plasma. The inability to adjust the "vacuum" layer thickness in the four-node poloidal divertor configuration allows only the conclusion that it was probably too large in these configurations. The proposed experiment on MST at the University of Wisconsin-Madison to vary the vacuum layer thickness should better quantify the allowable vacuum thickness. Future RFP designs will, no doubt, benefit from this knowledge.